

Review of single bunch instabilities driven by an electron cloud

F. Zimmermann*

CERN, AB Department, 1211 Geneva 23, Switzerland
(Received 19 August 2004; published 21 December 2004)

Electrons generated and accumulated inside the beam-pipe form an “electron cloud” that interacts with a charged particle beam. If the number of electrons is sizable, this beam-cloud interaction can give rise to a two-stream instability, resulting in beam loss or emittance growth. The instability can occur within a single bunch, e.g., passing through the cloud on successive turns in a storage ring, or it can be a multibunch instability, where the motion of successive bunches is coupled via the electron cloud. In this paper, I review the experimental evidence for, simulation approaches to, and analytical treatments of single-bunch two-stream instabilities caused by an electron cloud. Depending on the parameter regime, this type of instability may resemble a coasting-beam instability, classical beam breakup, or transverse mode coupling. It can also cause long-term emittance growth. Despite the apparent similarities, a few fundamental differences distinguish the two-stream instability from a conventional impedance-driven instability, and limit the applicability of established accelerator-physics concepts, like “wakefield.” On the other hand, if, in addition to the electron cloud, space-charge forces, conventional impedance, or beam-beam interaction are also present, these can conspire so as to enhance the growth rate.

DOI: 10.1103/PhysRevSTAB.7.124801

PACS numbers: 29.27.Bd, 29.20.-c, 52.35.Qz, 52.65.Tt

I. INTRODUCTION

Electron-cloud instabilities are a concern because they can lead to beam loss, emittance growth, and turn-by-turn or pulse-to-pulse trajectory changes. In this paper, I describe experimental evidence, simulation approaches, and analytical treatments for electron-cloud driven single-bunch instabilities. Some emphasis is placed on similarities with and differences from impedance-driven instabilities. I also discuss synergetic effects, e.g., the combined action of electron cloud and space charge or conventional impedance, and mention a few countermeasures against electron-cloud instabilities. A number of open issues are highlighted.

Although I here focus on single-bunch instabilities, it should be pointed out that these instabilities usually occur in multibunch or multiturn operation. In almost all cases, at least some electrons are present when a bunch arrives. This is particularly true for bunch trains with close spacing, where the electrons causing the instability are generated by the preceding bunches. For long proton bunches, as in the Los Alamos Proton Storage Ring (PSR), the electron density may greatly vary during the bunch passage, since here the so-called “trailing-edge multipacting” process results in a significant increase towards the tail of the bunch. As a consequence, for such long bunches the instability and the electron-cloud generation are more intimately connected, and, for example, the tail may become unstable first due to the much higher electron density it encounters.

Aside from instabilities with single-bunch character, the electron cloud can also drive true coupled-bunch instabil-

ities; these are discussed in a companion presentation by Ohmi [1]. Multibunch instabilities driven by an electron cloud were observed with positron beams at the KEK Photon Factory [2], at BEPC [3], and at KEKB [4], as well as with proton beams at the CERN SPS [5,6]. Simulations of the multibunch wakefields were reported first by Ohmi in [7] and further refined in [8]. Direct simulations of the instability were presented in [9,10], and a simplified analytical model of the multibunch instability was developed in [6]. Interestingly, recent simulation results by Schulte indicate that the bunch-to-bunch wakefields may likely excite higher-order coupled-bunch head-tail instabilities [11].

In the following section we describe various observations of single-bunch electron-cloud instabilities and the countermeasures which were implemented. We next discuss simulations and then proceed to analytical treatments. The review closes with some outstanding questions.

II. OBSERVATIONS

Perhaps the first ever observation of an electron-cloud driven instability was made with a bunched beam at a small proton storage ring of the INP Novosibirsk around 1965 [12–14]. The ring circumference was only 2.5 m. Coherent betatron oscillations and beam losses occurred above a threshold proton intensity of $1\text{--}1.5 \times 10^{10}$, as is illustrated in Fig. 1. Soon Budker and co-workers identified the instability as one due to electrons. It was cured by a transverse feedback system.

Two years later, another PSR at INP also suffered an electron-cloud instability, in this case with a coasting proton beam. The threshold here corresponded to 1.2×10^{11} protons, which were distributed over a 6 m circumference [15]. The coasting-beam instability was suppressed by

*Electronic address: frank.zimmermann@cern.ch

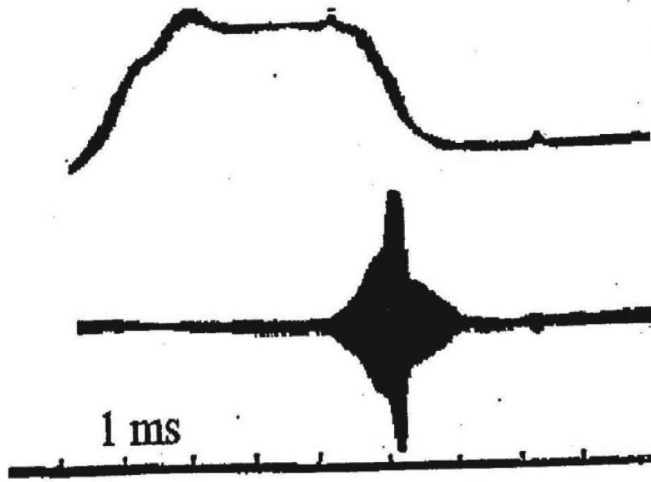


FIG. 1. Observation of an electron-driven instability at the INP PSR in 1965 [12]; beam intensity (top curve) and radial beam position (bottom curve) as a function of time (1 ms per division).

increasing the beam current and the gas density. This compensation scheme allowed storing up to 1.8×10^{12} protons, i.e., about 15 times the initial threshold value [14,16]. As pointed out by Dudnikov [14], the fast accumulation of secondary plasma by gas ionization was essential for the stabilization. The existence of an “island of stability” above the threshold was consistent with a previous analysis by Chirikov [17].

At about the same time as in Novosibirsk, a vertical instability, which is now attributed to electron cloud, was observed at the Argonne ZGS [14,18]; see Fig. 2. The instability growth time varied between 5 and 100 ms, and the intensity threshold from 2 to 8×10^{11} protons distributed over eight equally spaced bunches. It was observed that the most intense bunches also were the most unstable,

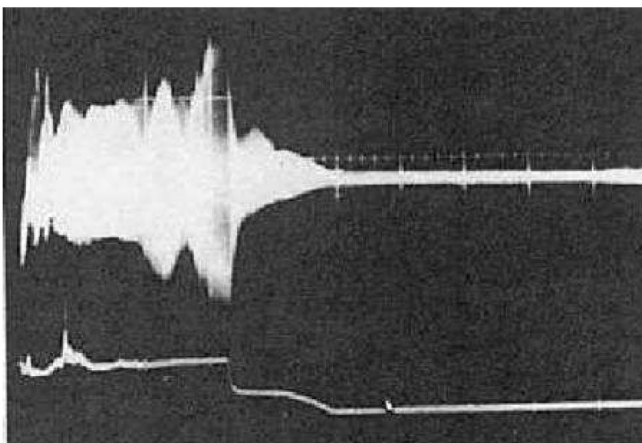


FIG. 2. Observation of coherent vertical instability at the Argonne ZGS in 1965 [18]; oscilloscope traces show the instability; the sweep rate is 0.2 s/cm; top trace: signal from a vertical pickup; bottom trace: beam current.

that the bunches moved independently from each other, that the threshold changed with the radial beam position (presumably due to nonlinear fields and an associated variation in Landau damping), and that the range or memory of the blowup did not extend for more than 70 feet around the machine. The instability was suppressed with a wideband (100 MHz) transverse damper [18,19].

Also, since 1965, an electron-related instability affected operation of the BNL AGS [20]. A typical observation from the AGS is displayed in Fig. 3. Again, a coherent vertical betatron oscillation led to beam loss. The instability could be caused by poor vacuum (10^{-5} Torr over 1/12 of the ring was sufficient to trigger the instability). A typical threshold current was 4×10^{11} protons per pulse, with 12 bunches. The instability growth rate strongly depended on the vacuum pressure. Growth times of 20–500 ms were common. Hence, the instability growth time was slow compared with the 8 ms synchrotron period. Pure modes of numbers n equal to eight and nine were found to be excited. At large amplitudes more than one mode was present. The instability was suppressed by increasing the chromaticity with sextupoles. A narrow band feedback was also developed, which proved partially successful in damping the instability. A wideband feedback remained under consideration for higher currents [20].

At about the same time, pressure-dependent instabilities were observed at Orsay. As noted by Bruck, these were attributed to nonlinear fields introduced by particles with a charge sign opposite to that of the beam (i.e., electrons or ions, depending on the beam charge) [20].

Given the history of electron-cloud instabilities in proton rings, perhaps it is not surprising that, in 1971, the Bevatron also suffered from an electron-driven instability, in this case for a coasting beam [21]. Defining the mode

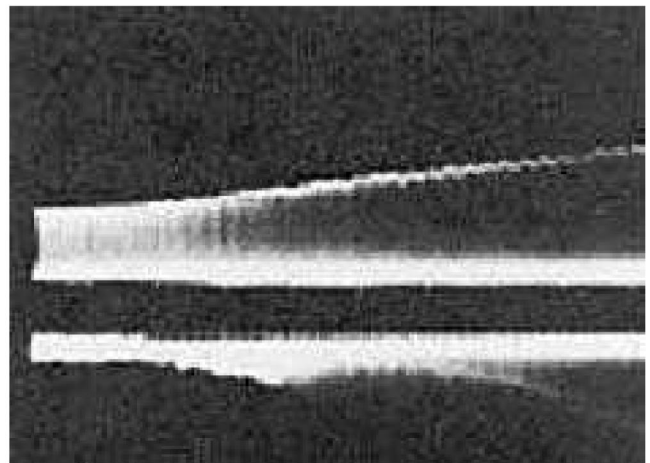


FIG. 3. Observation of coherent vertical instability at the BNL AGS in 1967 [20]; shown are the sum and difference signals from a vertical pickup; horizontal axis is time with 10 ms per division; the graph shows a 2 mm growth in peak-to-peak amplitude, at an intensity of 1.15×10^{12} protons.

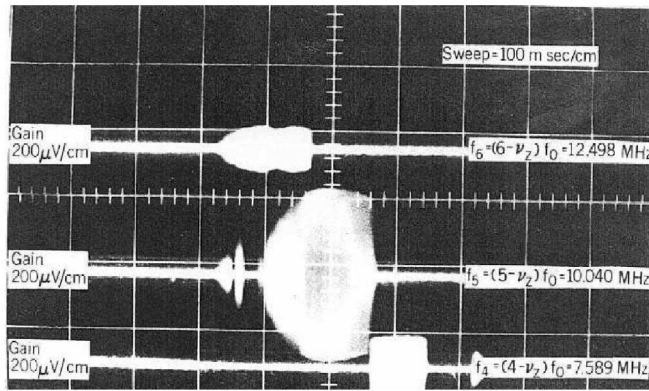


FIG. 4. Observation of a coherent coasting-beam instability at the Bevatron in 1971; oscilloscope traces show the amplitudes of modes 6, 5, and 4 as a function of time; sweep time is 100 ns per cm [21].

frequency by $f_n = f_0(n - Q_y)$, with the Bevatron revolution frequency f_0 of 2.455 MHz, all modes with n between three and ten were observed to become unstable, successively in time. The unstable mode number changed towards smaller values as the instability progressed, which was attributed to the decrease in the oscillation frequency of the electrons for increasing beam size. Figure 4 illustrates the cascade of excited modes in the Bevatron. For 10^{12} protons per pulse, the beam size doubled in 200 ms. The Bevatron vacuum pressure was 2×10^{-6} Torr. Clearing fields were applied. They decreased the oscillation amplitude by a factor of 2. The instability was not very sensitive to the settings of the octupoles. A detection and feedback system was built, which stopped the growth of the beam size, but resulted in non-negligible steady-state oscillations. The general behavior of the feedback was somewhat erratic, since it was optimized for a single mode ($n = 6$) only.

The observation of electron-cloud instabilities in coasting beams at the CERN ISR has by now become legendary. A measurement from 1972 is presented in Fig. 5. The instability had a fast rise time and lasted for 5–10 ms. It repeated itself, e.g., in intervals of 1–2 s. The ISR instability was thought to transport protons into nonlinear resonances. In addition, it was suspected that successive electron-proton instabilities led to a gradual beam blowup similar to multiple scattering off the residual gas. For a pressure of 2×10^{-11} Torr, a neutralization level of 3.5% was estimated, corresponding to a tune shift (or tune modulation amplitude) of about 0.015 [22]. An extensive system of electrostatic clearing electrodes was installed to keep a low residual neutralization level.

Since about 1988, an electron-cloud instability has been observed at the Los Alamos PSR [23,24]. The characteristics of the instability are similar to those at the earlier proton storage rings. A coherent vertical betatron oscillation starts, grows, and results in beam loss, as illustrated in

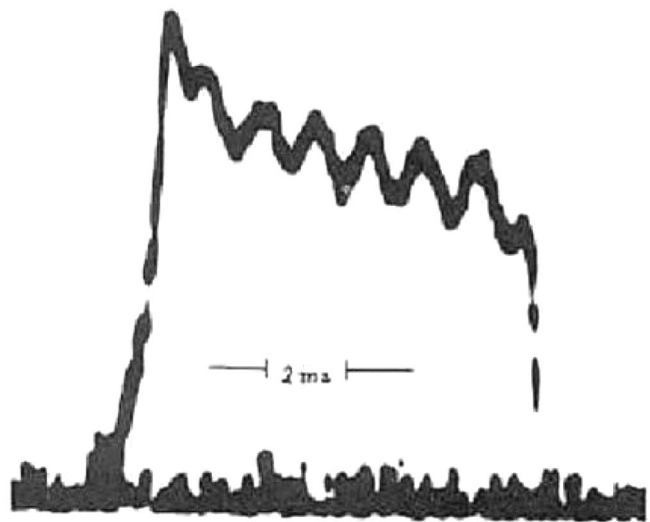


FIG. 5. Observation of coupled electron-proton instability at the CERN ISR in 1972 [22]; shown is the beam-induced signal from a horizontal pickup; the coasting beam current was 12 A and the beam energy 26 GeV. A horizontal span of 2 ms is indicated.

Fig. 6. The beam loss occurs on a time scale of 10–100 μ s above a threshold charge of 1.5×10^{13} protons. The LANL PSR ring circumference is 90 m, and the harmonic number 1. The transverse oscillations during the instability exhibit a frequency around 10 MHz.

Figure 7 shows the same type of signal on a different time scale, namely, recorded over two successive turns.

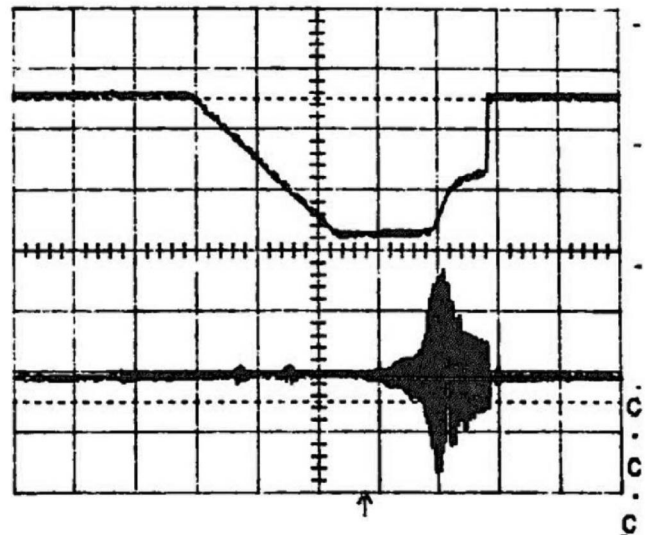


FIG. 6. Observation of coherent vertical oscillation and the resulting beam loss at the Los Alamos PSR instability around 1990 [23]; beam current (top curve shows inverted signal from beam current monitor) and vertical oscillations (bottom curve is the simultaneous signal from a vertical difference monitor); horizontal axis is time with 200 μ s/div.

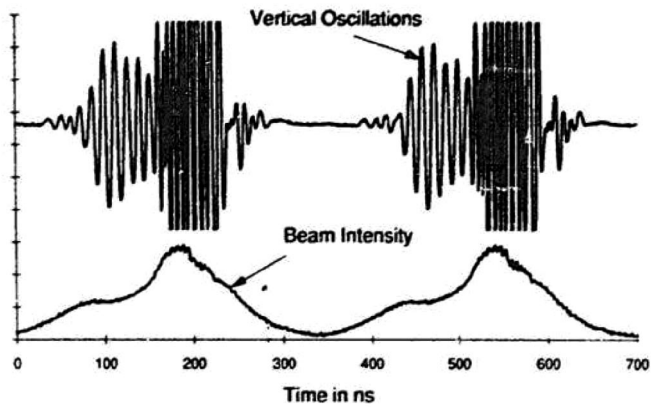


FIG. 7. Observation of PSR instability signals over two successive turns [23].

The frequency of the oscillation clearly varies along the bunch, roughly as the square root of the local line density. Lower-amplitude lower-frequency oscillations are associated with the “shoulder” of the bunch profile.

The square-root dependence of the frequency on the charge density was also seen when comparing instability frequencies for different bunch populations, lending early support to the hypothesis that the instability was of the “ $e-p$ ” type [23]. In addition, changes in instability frequency were monitored over a single cycle. Figure 8 illustrates the evolution of the beam spectra as the instability progresses.

Two important features of the PSR instability are that the maximum number of protons at the threshold scales linearly with the rf voltage and that it is almost independent of bunch length, as is illustrated in Fig. 9. A conditioning with operation time has been observed, as is indicated by the “historical” curve in Fig. 9. Other characteristics of the PSR instability are the occurrence of sustained coherent oscillations below the loss threshold and the observation of an intense electron flux on the wall at the end of a bunch passage. The latter can be seen in Fig. 10, which also illustrates the progression of the instability from the end of the bunch towards the front, suggesting that for the PSR electron production and instability should be considered as a combined process.

Around 1989, Blaskiewicz performed a series of electron-cloud experiments at the BNL AGS booster [25]. He was able to intentionally produce a coasting beam electron-proton instability, which is illustrated in Fig. 11. Figure 12 shows a downward frequency shift by about 100 MHz as the instability progresses.

It also was in 1989 that the KEK Photon Factory switched from electron to positron operation. The positron beam suffered from a wideband vertical multibunch instability which had not been seen with electron beams [2]. The unstable mode pattern of this instability was characteristic of a wakefield extending only over a few bunches. It varied with the beam current. The instability was inter-

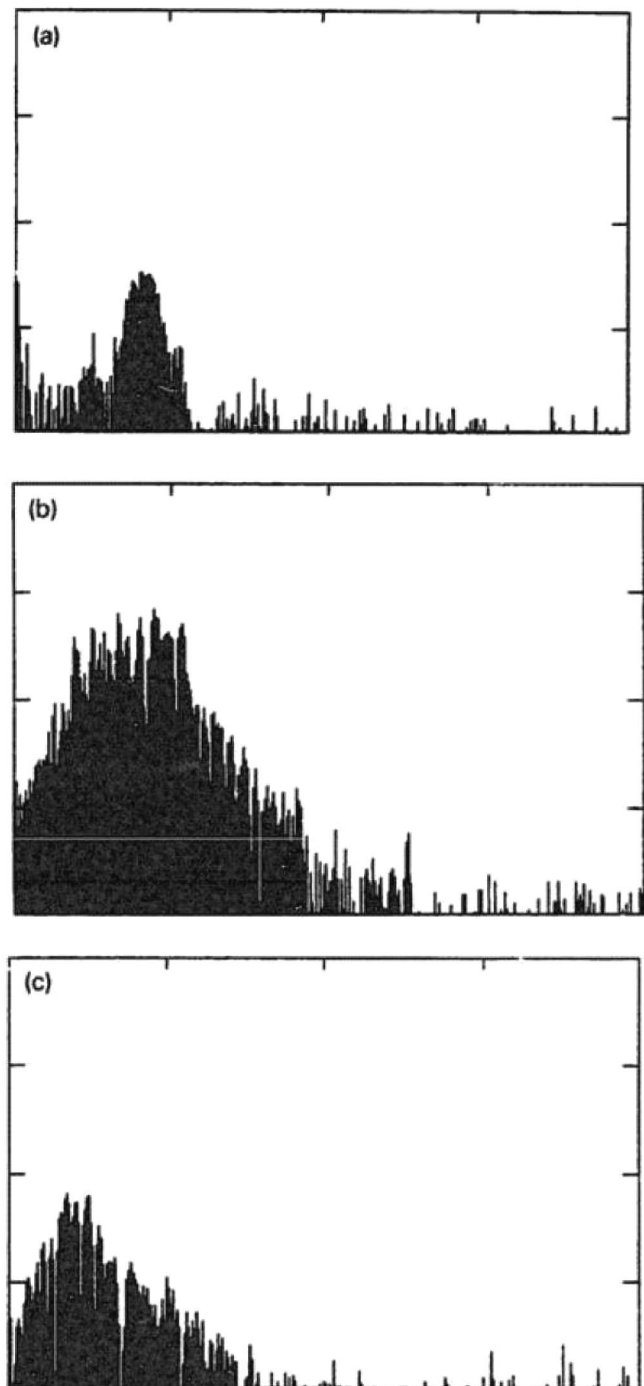


FIG. 8. Spectra recorded during a single PSR cycle with a strong instability [23]; (a) shows the spectrum at the beginning of the instability, (b) 100 μ s later, and (c) 300 μ s later after beam loss; the vertical scale is logarithmic; the horizontal span extends from 0 to 1 GHz.

preted as one driven by photoelectrons [2]. By applying a clearing voltage of ± 2.5 kV to all 88 beam-position monitors (BPM) around the ring the vertical beam size was reduced by 15%, though the instability was not completely suppressed [2]. In an attempt to model this phenomenon quantitatively, detailed computer simulations of the elec-

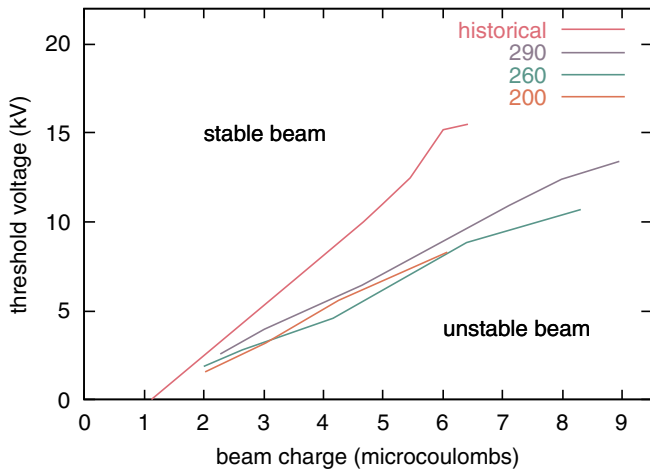


FIG. 9. (Color) PSR threshold rf voltage versus bunch intensity [80]; the historical curve reflects the situation before the extended 2001 run, the other three curves refer to three different injected bunch lengths (200, 260, and 290 ns) at the end of this run.

tron buildup inside a vacuum chamber and the resulting wakefield were performed [7]. This investigation at the KEK Photon Factory was probably the first one which revealed an electron-cloud effect for lepton beams, and it ushered in the “modern era” of the effect, sparking substantial and widespread interest.

In 1999 it was observed that the beam size of the KEKB positron beam, consisting of many closely spaced bunches, strongly blew up above a certain threshold current [26]. At the end of 1999 it was suggested that the blowup was a manifestation of a single-bunch electron-cloud instability,

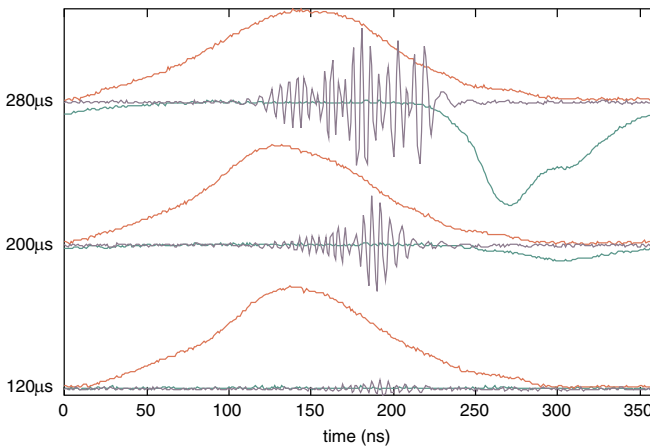


FIG. 10. (Color) Evolution of the vertical PSR instability; red Gaussian-like trace is the beam current, blue oscillating trace the vertical beam position (difference signal), and the green negative curve the electron current measured by a detector at the wall; from bottom to top the traces were obtained 120, 200, and 280 μ s after the end of accumulation; the beam charge is 4.4 μ C.

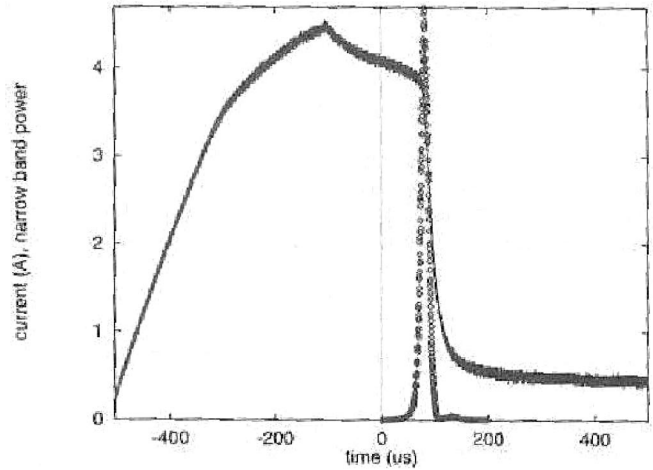


FIG. 11. Coasting-beam vertical instability at the BNL AGS booster in 1998/1999 [25]; shown are the beam current in units of A and the vertical narrow band power density at 76 MHz (smoothed over one turn); the horizontal span ranges from -500 to 500μ s.

similar to conventional beam breakup or transverse mode coupling instability (TMCI) [27,28], where small beam perturbations are amplified by the electron cloud as by a wakefield. Unlike for the proton accelerators the primary source of electrons in the KEKB positron ring are photoelectrons, which are generated by synchrotron-radiation photons impinging on the vacuum-chamber wall. Installation of solenoids, starting in the summer of 2000, increased the current threshold. The beneficial effect of the first set of solenoids is demonstrated in Fig. 13. There also is some evidence for a slower, more gradual blowup, below

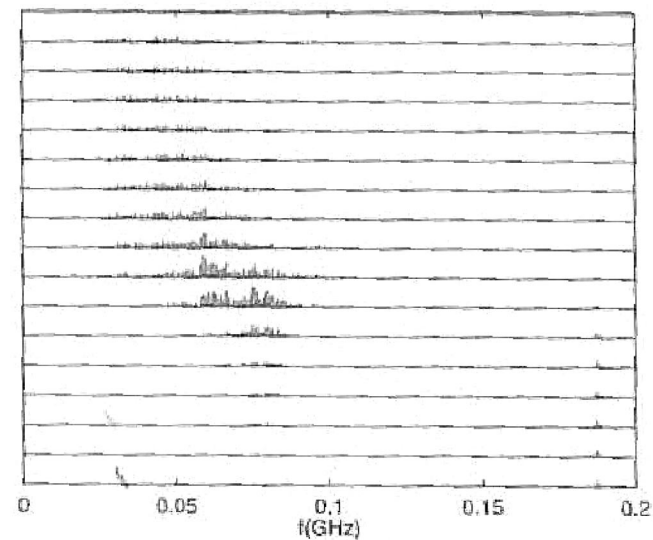


FIG. 12. Shift in AGS-booster vertical beam spectrum as the instability progressed [25]; the time advances from the bottom to the top (12 μ s between traces); the vertical scale extends from 0 to 0.2 GHz.

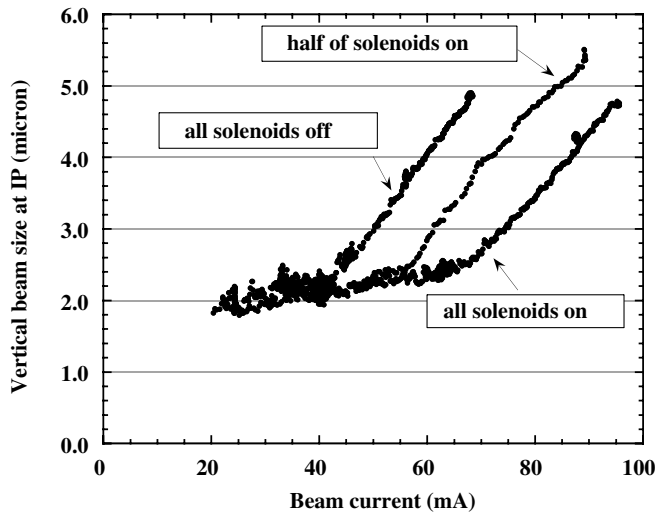


FIG. 13. Vertical beam size of the KEKB LER positron beam as a function of the beam current measured by the synchrotron-light interferometer in 2000 [95]; two trains with 60 bunches each were injected on opposite sides of the ring; the bunch spacing was four rf buckets; the effect of the first set of solenoids covering an effective length of 800 m is shown.

the threshold of the steep beam-size increase. It is not clear if this gradual beam-size increase reflects the effect of a different process blowing up the beam (perhaps similar to the slow blowup seen in recent simulations of Benedetto for the LHC [29]), or if it is an instrumental artifact of the beam-size measurement.

Following a proposal by Perevedentsev, the single-bunch nature of the fast blowup was studied by injecting a test bunch immediately behind a train of bunches and varying the charge of this test bunch, keeping the charge of the preceding bunches constant. The result of this measurement is illustrated in Fig. 14, which shows that the size of the test bunch increased when its bunch current was increased. This blowup, therefore, is a single-bunch effect [30].

Preliminary attempts were made at KEKB to detect the head-tail motion of individual bunches using a streak camera in dual-sweep mode. Figure 15 shows an example measurement from around 2002, without solenoid field. Bunches in the tail of the train are blown up vertically, and there may also be some evidence for a head-tail tilt in a few of them. Further and more recent streak-camera measurements were presented by Fukuma in Ref. [31].

At KEKB the primary countermeasure has been the confinement of photoelectrons to the vicinity of the vacuum-chamber wall by an extensive installation of solenoids in all field-free regions of the ring [30] (the remedial effect of the solenoids is evident in Fig. 13). A multibunch feedback system is always active at KEKB. At least in the early years, the blow could be reduced by a large chromaticity, e.g., up to $Q' \approx 12$ [30].

In the summer of 2000, a beam size blowup due to electron cloud, similar to that at KEKB, was also noticed

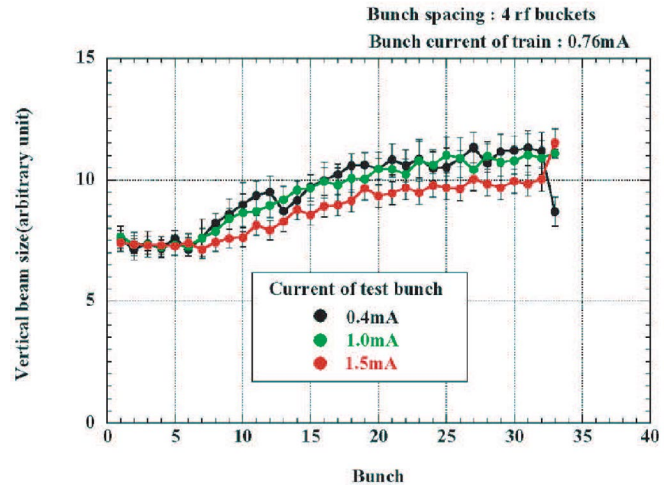


FIG. 14. (Color) Vertical beam size along a train followed by a test bunch in the KEKB LER, as observed by a synchrotron-light monitor with a gated camera, versus the bunch number [30]; the three curves refer to three different currents of the (last) test bunch, as is indicated in the legend.

at the SLAC PEP-II B factory. Figure 16 illustrates this blowup for a single noncolliding beam, as seen on a synchrotron-light monitor. Different from KEKB, at PEP-II the horizontal beam size also increased as a function of current, and even more strongly than the vertical. The reason for the different behavior at the two B factories is not understood, but, as described below, the working point in tune diagram seems to play a role.

The PEP-II blowup occurred in collision as well. This is illustrated in Figs. 17 and 18. Figure 17 displays the

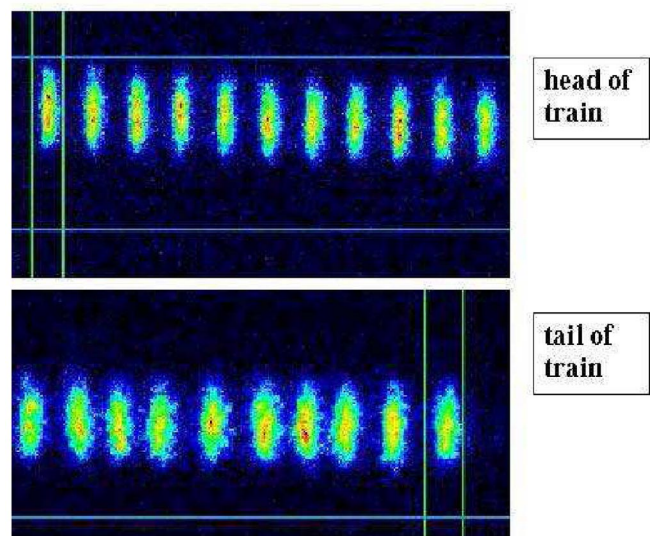


FIG. 15. (Color) Streak-camera measurement in dual-sweep mode of individual vertical beam sizes and their y - z correlation at KEKB [103]; the vertical axis is the time along the bunch, the horizontal axis the vertical direction; consecutive bunches are displayed, separated horizontally.

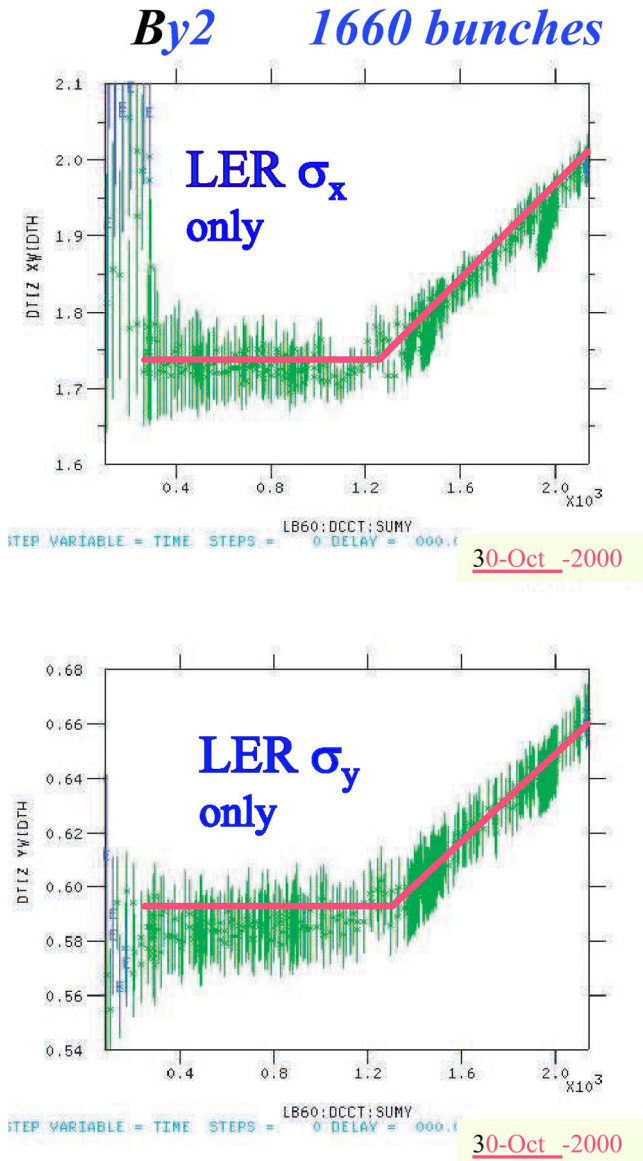


FIG. 16. (Color) Horizontal (top) and vertical beam size (bottom) of the PEP-II positron beam measured by synchrotron-light monitor on October 30, 2000, as a function of the total beam current in mA [104]; the horizontal scale extends from about 0.15 to 2.15 A; the beam consisted of 1660 bunches spaced by two rf buckets.

luminosity as a function of bunch number along several long trains. The luminosity drops by more than a factor of 2 towards the end of each train, which was attributed to the electron-cloud induced beam-size blowup. Figure 18 shows a direct measurement of the blowup with colliding beams. In this example, minigaps of two missing bunches were introduced to clear the electrons between short trains comprising 22 bunches each. Two components of the beam-size blowup are visible: An increase by about 50% with respect to the single-beam size, attributed to the beam-beam interaction, and a further increase by up to 20% along each minitrain, due to the electron cloud.

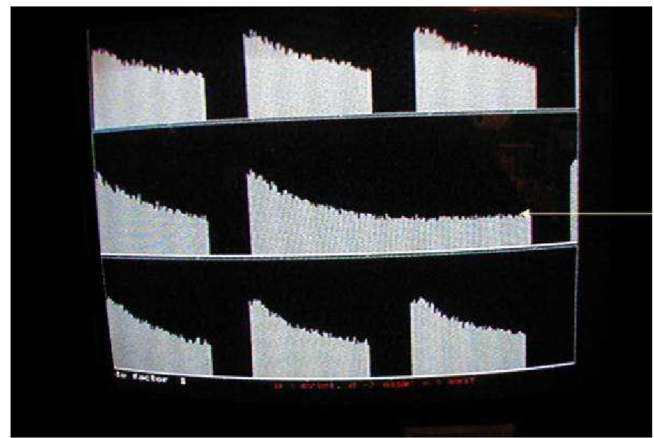


FIG. 17. (Color) Luminosity versus bunch number recorded at the PEP-II B factory in July 2000 for a bunch spacing of four rf buckets with eight additional large gaps [104]; only one straight solenoid was installed at this time. The three traces, when strung together from top to bottom, represent one full turn.

In May 2003, the tunes of the PEP-II LER were shifted away from the third integer resonance closer to the integer. This change in tune is illustrated in Fig. 19. After the tune change the electron-cloud induced horizontal blowup dis-

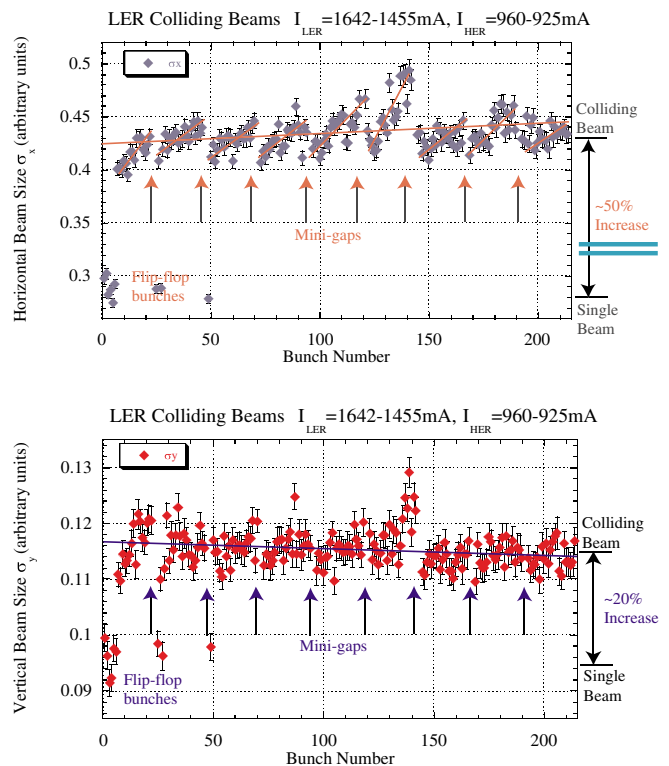


FIG. 18. (Color) Horizontal and vertical beam size as a function of bunch number with colliding beams at the PEP-II LER in 2001 [104]; the measurement was taken by a gated camera, with an LER bunch current of 2.0 mA (HER bunch current 1.25 mA); short 22-bunch trains were separated by minigaps of two missing bunches; the bunch spacing was four rf buckets.

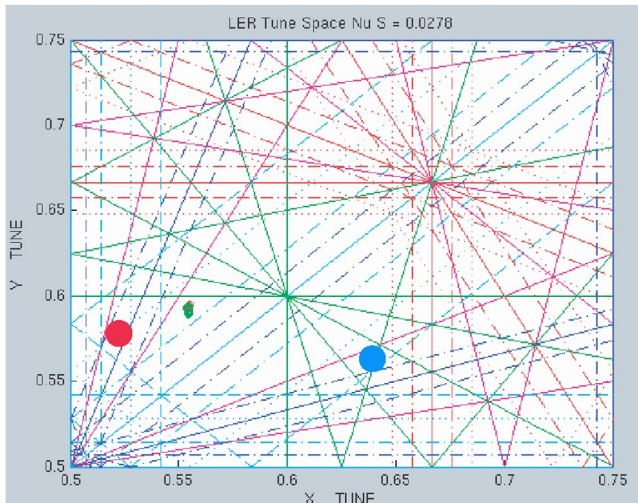


FIG. 19. (Color) Change in the PEP-II LER nominal working point from $(Q_x, Q_y) = (0.64, 0.56)$ (blue) to $(0.52, 0.57)$ (red) on May 1, 2003 [32].

appeared for the colliding beams. The positron beam size now only depends on the electron-beam current, and hence it is dominated by the beam-beam interaction [32]. By contrast, until this time it had mainly been correlated with the positron beam current itself. The electron-cloud (and beam-beam?) effect in PEP-II thus appears quite sensitive to the working point, which might well account for some of the differences from KEKB.

During the construction of the accelerator the PEP-II arc vacuum chambers were coated with TiN in order to reduce the secondary emission yield. Antechambers absorb most of the synchrotron radiation. Nevertheless, a significant electron cloud was observed. Measurements of electron flux at the wall suggest that in PEP-II the electrons are generated primarily by beam-induced multipacting (despite the TiN coating). PEP-II uses a multibunch feedback, which damps the bunch centroid motion. An intrabunch feedback is under development for higher beam current [33]. The main remedies to suppress electron-cloud effects were the installation of solenoids, as in KEKB, and the tailoring of the bunch filling pattern, e.g., introducing minigaps plus charge ramps along trains.

Since 1999, an LHC test beam has been available in the CERN SPS, which is being upgraded to serve as the LHC injector. The LHC beam is composed of trains of 72 proton bunches spaced by 25 ns, with a bunch population of 1.15×10^{11} . In the SPS, this beam will be accelerated from the injection momentum 26 GeV/c to the extraction momentum of 450 GeV/c. Already in 2000, early SPS machine experiments with the LHC beam revealed emittance growth and beam loss above a certain current threshold that coincided with the thresholds of a large pressure increase and of a significant electron flux on the chamber wall. An example of beam loss in the tail of a bunch train after injection is shown in Fig. 20.

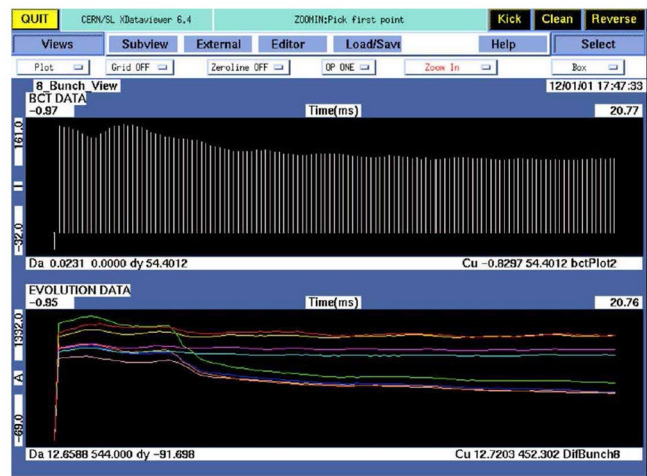


FIG. 20. (Color) Intensity of the LHC beam versus time after injection at the CERN SPS in 2000: relative total intensity (top) and relative bunch intensity for four bunches at the start and in the tail of the train (bottom) [5]; losses after a few ms are visible for the trailing bunches; the intensity was measured every seven turns for a span of about 20 ms.

The character of the SPS instability is different in the two transverse planes [5,6]. In the horizontal plane a low-order coupled bunch instability is observed, with all bunches oscillating approximately in phase. In the vertical plane the instability shows single-bunch character, without any phase or amplitude correlation between successive bunches. At high intensity the growth time is about 50 turns (roughly 1 ms) in both planes. The vertical growth rate is more sensitive to the beam current. Snapshots of the horizontal and vertical beam positions for the first 48 bunches in a train during instability are displayed in Figs. 21 and 22.

The SPS instabilities were suppressed by the transverse feedback (“damper”) and high chromaticity (up to $\xi_y \equiv Q'_y/Q_y > 1$) in both planes. Another approach of weakening the instability, suggested by Métral and not yet tested, is to increase the linear coupling [34]. In the SPS, both the beam stability and the vacuum-pressure increase due to electron cloud were much improved after about two weeks

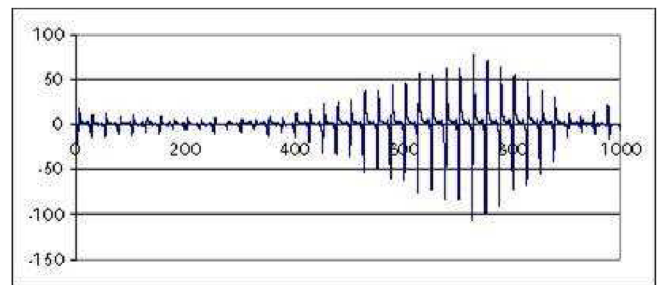


FIG. 21. (Color) Snapshot of horizontal position of the first 48 bunches in the SPS when the instability is present [6].

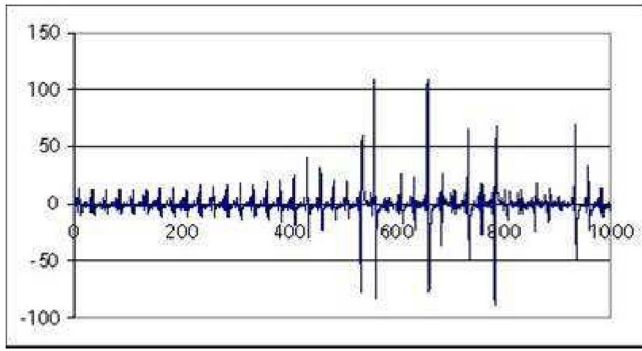


FIG. 22. (Color) Snapshot of vertical position of the first 48 bunches in the SPS when the instability is present [6].

of a dedicated scrubbing run with high pressure and high duty cycle, but a residual effect remained. The interaction of the electron cloud with the conventional vacuum-chamber impedance and possibly space charge is thought to be important in the vertical plane.

Measurements of the horizontal tune shift with amplitude evidence a significant detuning which is positive at low amplitudes ($\Delta Q \approx 0.01$ at 1σ) and negative at larger amplitudes [35]. A hysteresislike behavior is also visible, as the amplitude decreases again (Fig. 23). The detuning and hysteresis may be related to the nonlinear character of the wake coupling successive bunches and/or they may reflect the local distribution of the electron cloud including its pinch during a bunch passage.

The SPS instability is different in the two planes of the SPS, since the electron cloud is concentrated in regions with dipole magnetic fields. Here electrons can freely move up and down along the field lines during a bunch passage, while they are constrained in the horizontal di-

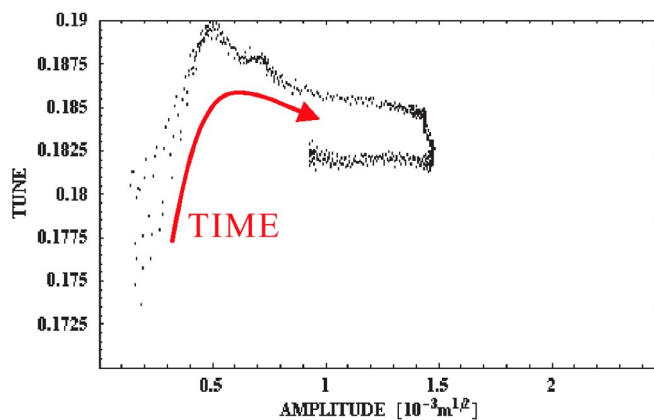


FIG. 23. (Color) Tune versus normalized oscillation amplitude at the tail of the LHC bunch train in the SPS for a bunch population of 1.1×10^{11} [35]; the data for the first 700 turns after injection are plotted; each data point represents a sliding-window average over 32 successive turns of the amplitude and phase advance per turn.

rection. The attraction of the electrons in the vertical plane leads to a “pinch” enhancement of the local electron density inside the beam. The electron cloud is then expected to give rise to an effective wakefield, whose strength varies along the bunch. A characteristic frequency of this electron cloud “wake” is the oscillation frequency of the electrons in the bunch potential. At the SPS nonrigid vertical head-tail oscillations can be detected by a wide-band pickup resolving the transverse beam position over a fraction of about 1 m full bunch length. Kicking the beam transversely, the evolution of the betatron phase difference can be detected as a function of the turn number. Originally this detector was designed for fast chromaticity measurements. However, the head-tail phase is sensitive not only to chromaticity, but also to conventional impedance and to the electron cloud. Figure 24 shows the measured head-tail phase difference for a bunch at the head of the train (without electron cloud) and for a bunch at the end (with electron cloud). Clearly the electron cloud induces an additional frequency in the signal. The measured electron-cloud contribution can be reproduced in calculations, if a wakefield with interaction length equal to 0.3–0.5 times the full bunch length is introduced to model the electron-cloud head-tail coupling [6,35]. The SPS measurement, therefore, provides a direct evidence for the existence of head-tail instability.

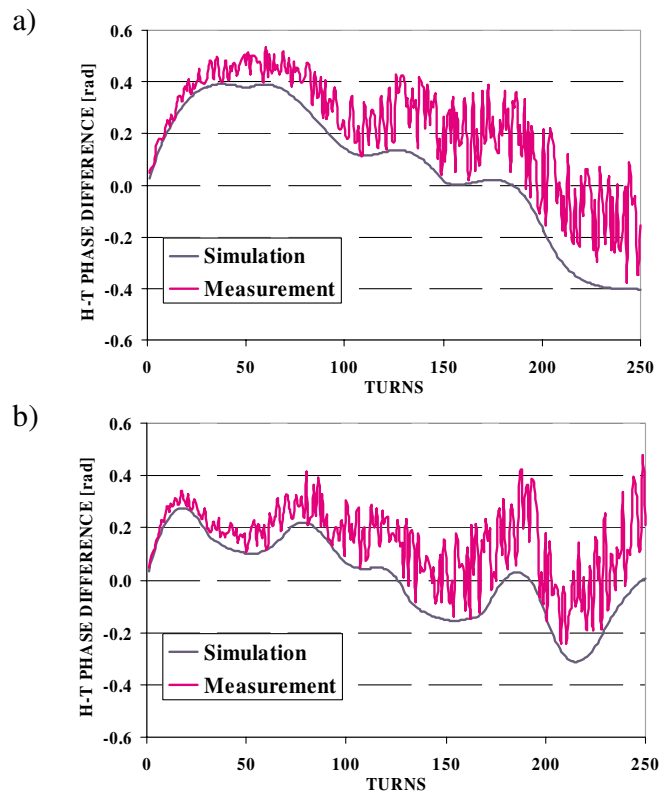


FIG. 24. (Color) Calculated and measured head-tail phase difference for a bunch in the head (a) and a bunch in the tail (b) of the LHC bunch train [6,35].

After it was observed that the LHC beam in the SPS suffered from electron-cloud instabilities, it was attempted to create an electron cloud in the CERN PS, where the LHC beam is produced before it is injected into the SPS. The electron cloud in the SPS is generated by beam-induced multipacting, a process which requires a sufficiently short bunch length. For the initial full length of 16 ns, no electron cloud is observed in the PS. However, prior to their extraction, the PS bunches are shortened from 16 to 4 ns (full length) using a fast bunch rotation. The short bunches stay in the ring only for a few tens of turns. For study purposes, a different adiabatic rf gymnastics was applied in 2000, which allowed shortening the bunches to 10 ns, while keeping them in the PS ring for about 100 ms. Indeed, in this case a fast horizontal instability was observed above a threshold bunch population of 4.6×10^{10} [36,37], as is illustrated in Fig. 25. Above the threshold the instability rise time was almost constant, equal to 3–4 ms, but the instability started earlier in time the higher the bunch charge. For the three highest intensities shown in Fig. 25, the bunches were still longer than 10 ns at the onset of the instability. It is remarkable that the instability occurred only in the horizontal plane (possibly due to the PS

combined function magnets) and that it gave rise to persistent large oscillations, without beam loss.

Figure 26 provides some further information on the PS instability. Together with the growth rate in the ring, it shows the Fourier spectrum over a wide frequency range, indicating that many betatron lines participate in the instability, and the single-passage signal from transverse beam-position pickups in the ring and in the transfer line. Especially the last figure demonstrates that the instability is present only in the horizontal plane and that there is no regular pattern in the horizontal position along the bunch train. This seems to rule out a multibunch instability.

A number of impressive experiments on electron-cloud effects were performed at BEPC, starting in 1996 as an IHEP-KEK collaboration for KEKB, and in more recent studies focusing on the BEPC-II upgrade. In operation with a single positron beam both coupled-bunch instabilities and a “single bunch” beam-size blowup are observed [38]. Figures 27–30 illustrate the suppression of the single-bunch blowup which was achieved by increasing the chromaticity, by exciting solenoid fields in the field-free regions to 15 G or a single octupole to 30 m^{-3} (corresponding to 1 A), or by biasing all 128 buttons of the 32 ring BPMs at a voltage of $\pm 600 \text{ V}$, respectively.

Figure 31 shows some raw beam-size measurements, for the effect of a BPM bias. These results from BEPC might represent the first successful application of clearing electrodes for suppressing the single-bunch beam blowup due to an electron cloud. We caution that in Fig. 30 the sizes of both head and tail bunches are reduced by the BPM bias, which could indicate a small optics difference, and that Fig. 31 suggests the presence of longitudinal oscillations. Comparing the efficiency of the different remedies explored, Guo and co-workers inferred from the BEPC experiments that the solenoids reduced the vertical size of a

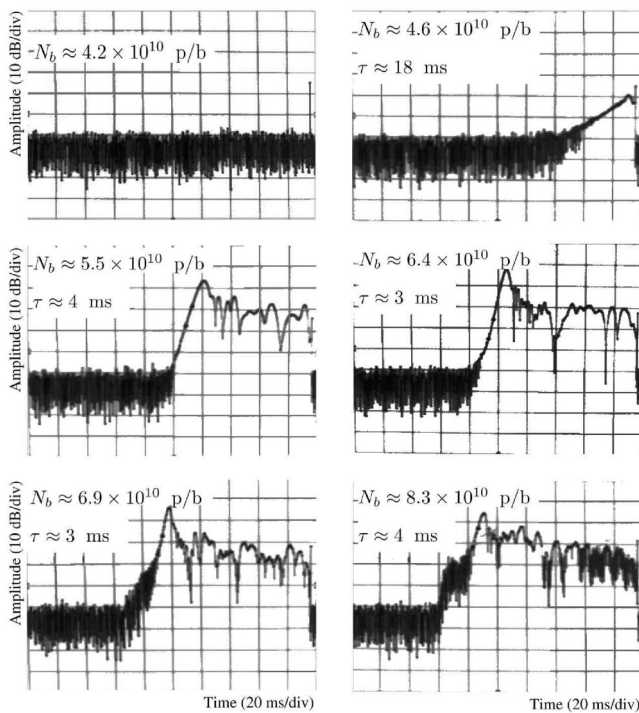


FIG. 25. Time evolution of the first unstable betatron line during electron-cloud experiments at the CERN PS in 2001 [36]; the LHC bunches are shortened at a constant length for the last 100 ms; the horizontal axis is time with 20 ms per division; the various pictures refer to different bunch populations, increasing from 4.2×10^{10} to 8.3×10^{10} ; the signal was obtained by a spectrum analyzer with zero span and central frequency set to 357 kHz.

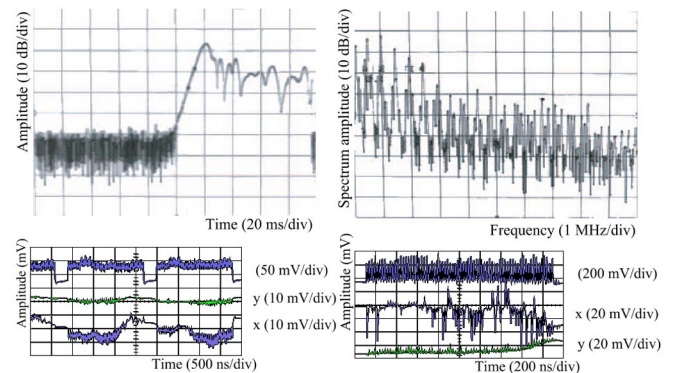


FIG. 26. (Color) Instability footprint for a bunch population of 5.5×10^{10} in the CERN PS [36]; the signal obtained from a spectrum analyzer with zero span (upper left picture), Fourier analysis from 0 to 10 MHz (upper right), signal from a pickup in the PS ring several tens of ms before extraction (bottom left) and from a pickup in the PS-to-SPS transfer line (bottom right).

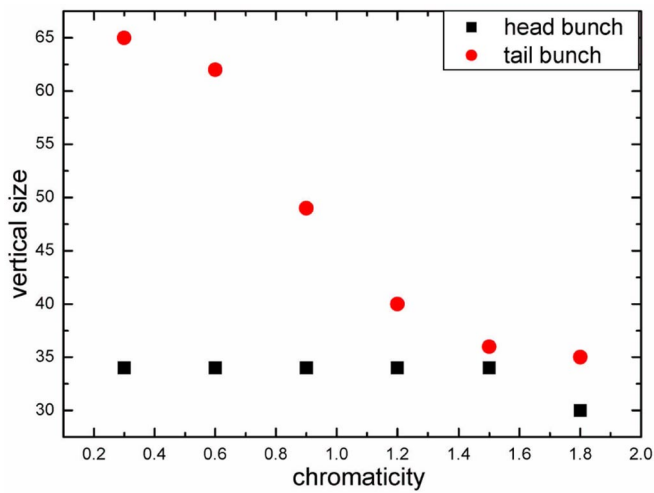


FIG. 27. (Color) Vertical beam size of the first and last bunch in a train as a function of chromaticity at BEPC in 2004 [38]; the beam size was measured by a streak camera.

tail bunch by 27%, the BPM bias by 18%, the octupole by 34%, and the chromaticity by 46% [38].

It has long been a mystery why DAFNE did not see an electron-cloud effect, unlike the two B factories and BEPC. However, recently a horizontal instability with a low threshold, where electron cloud may play a role, was observed for the positron beam only [39]. Betatron amplitudes were measured turn by turn and bunch by bunch. Figures 32 and 33 show the result of grow-damp measurements, in which the feedback was switched off for a short time. As can be seen, the instability growth rate strongly increases along the bunch train, similar to what might be expected from an electron-cloud buildup along the train or from a short-range wakefield coupling successive bunches.

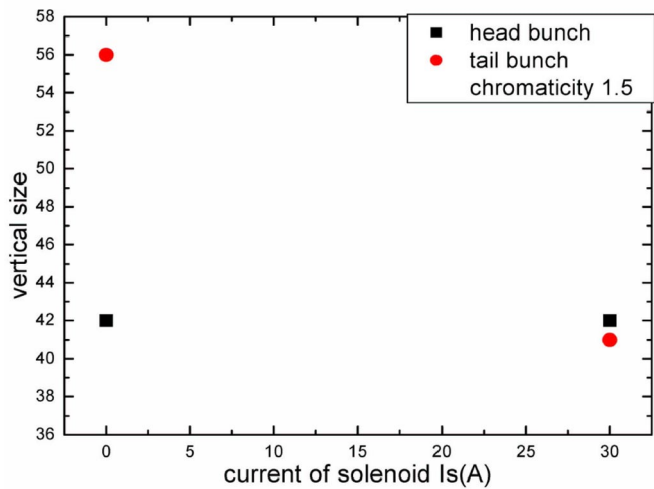


FIG. 28. (Color) Vertical beam size of the first and last bunch in a train as a function of the solenoid strength at BEPC in 2004 [38]; the beam size was measured by a streak camera.

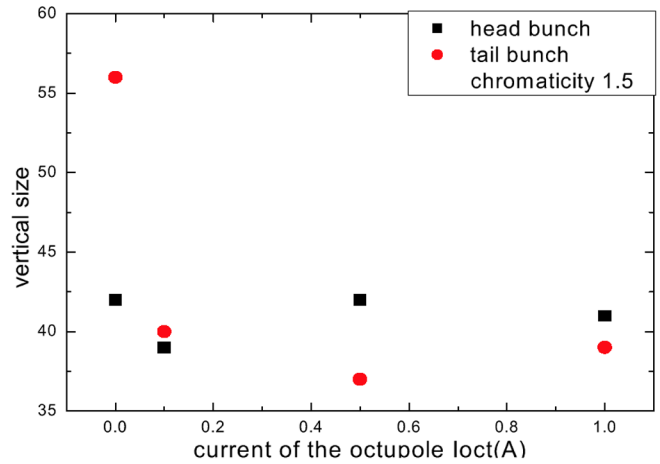


FIG. 29. (Color) Vertical beam size of the first and last bunch in a train as a function of the octupole strength at BEPC in 2004 [38]; the beam size was measured by a streak camera.

A series of complementary measurements were performed. Single-bunch tune shifts with current are negligible for both electron and positron rings. While for electrons the multibunch tune shifts have slopes of opposite sign in the two transverse planes and can be calculated analytically (the strong asymmetry is due to the wiggler vacuum chamber), for the positron ring the vertical tune shift is almost zero, but the horizontal one is positive and by a factor of 2 higher than that in the electron ring. The instability threshold in 2004 after reducing the nonlinear fields in the wiggler magnets was a factor of 2 lower than in the fall of 2003. The threshold corresponds to a tune shift approximately equal to the synchrotron tune, indicating transverse mode coupling (TMC) instability as a likely source. The wake could be due to an electron cloud, resistive wall, cavity higher-order modes (HOMs) or, likely, a combina-

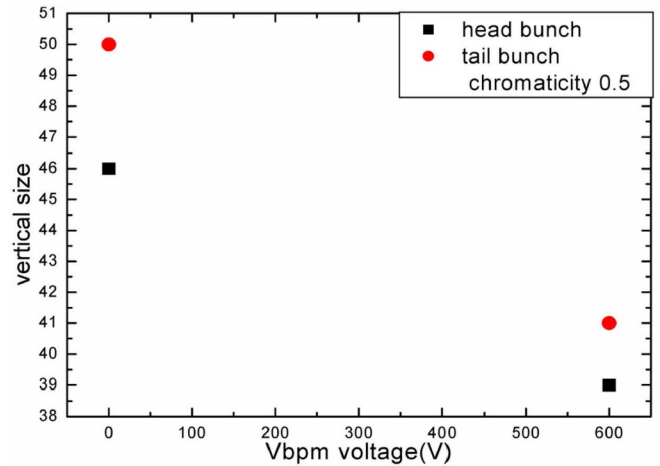


FIG. 30. (Color) Vertical beam size of the first and last bunch in a train as a function of the BPM bias voltage at BEPC in 2004 [38]; the beam size was measured by a streak camera.

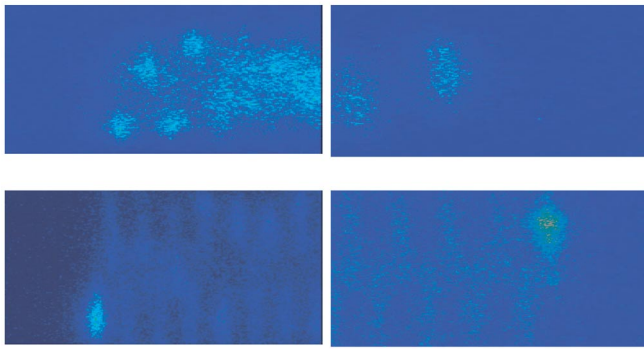


FIG. 31. (Color) Streak-camera measurement in dual-sweep mode of individual vertical beam sizes and their y - z correlation at BEPC [38]; bunches in the head (left) and tail of the train (right) are compared without (top) and with ± 600 V bias at all 128 BPM buttons (bottom); the vertical axis is the time along the bunch, the horizontal axis the vertical direction; consecutive bunches are displayed, separated horizontally.

tion thereof. The threshold is unexpectedly sensitive to the rf frequency. This sensitivity is possibly related to changes in Landau damping. The instability does not occur with colliding beams. Presumably, in collision it is suppressed by the additional beam-beam tune spread.

After reviewing the long history of electron-cloud single-bunch instabilities in proton and positron accelerators, we could ask if there has been any significant progress

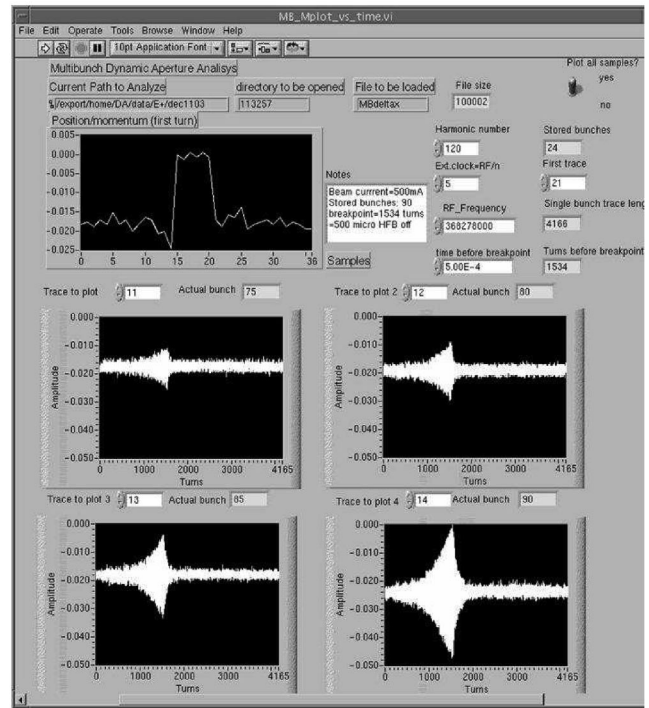


FIG. 33. Grow-damp measurement of horizontal oscillations for bunches 75, 80, 85, and 90 at DAFNE in 2004 [39]; the feedback was switched off for a short time; 90 consecutive bunches were followed by a gap of 30 missing bunches.

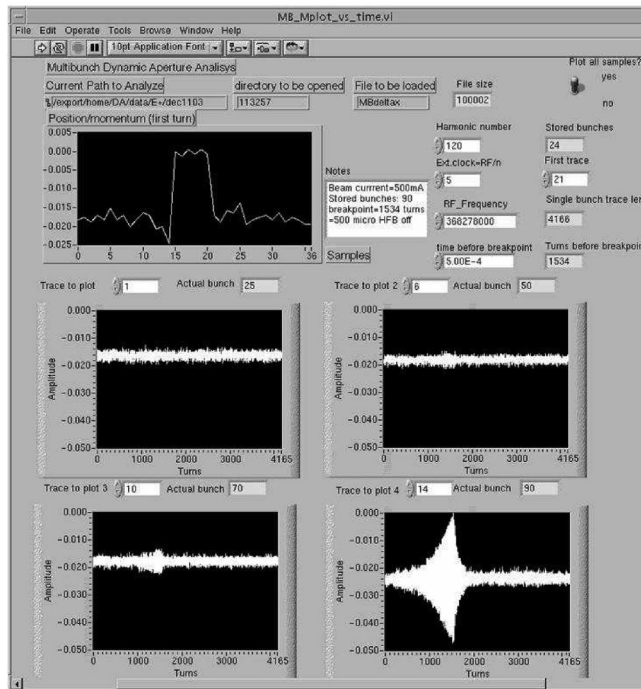


FIG. 32. Grow-damp measurement of horizontal oscillations for bunches 25, 50, 70, and 90 at DAFNE in 2004 [39]; the feedback was switched off for a short time; 90 bunches were followed by a gap of 30 missing bunches.

after 40 years of studying this phenomenon. It appears to me that the same cures have been applied from the earliest observations in the mid-1960s until today. These common cures include the change of chromaticity, the use of octupoles, wideband and/or narrow band transverse feedbacks, clearing electrodes, and improving the vacuum pressure. The only new approach seems to be the application of TiN or TiZrV getter coating. The practical efficiency of the TiN coating at PSR and PEP-II appears somewhat questionable, while the first experience with TiZrV at the SPS is encouraging. The only other true progress that I can observe is the clear identification of the electron cloud as the root cause for instabilities and beam-size blowup in many machines, thanks to much improved diagnostics, and the improved models of electron generation and resulting instabilities, which benefit from the greatly enhanced computing power. However, despite 40 years of studies, lots of questions remain to be answered.

III. SIMULATIONS

Computer simulations appear indispensable for a proper prediction and understanding of the instability dynamics. In the simulations, various different approaches are followed to model the interaction of a bunch and an electron cloud:

- (i) representing the beam by a number of microbunches with finite transverse size, but pointlike in the longitudinal

phase space, and the electrons by macroparticles; the force on the electrons is computed for each microbunch separately, using the classical Basetti-Erskine formula for the field of a Gaussian charge distribution; the force on the microbunches is obtained via the action-reaction principle (Ohmi's PEHT code [28], Cai's ECI code [40]);

(ii) using a soft-Gaussian approximation (Rumolo's HEADTAIL code version 0 [41]);

(iii) discrete PIC codes (Ohmi's code PEHTS [42], Rumolo's code HEADTAIL [41,43], code from IHEP [38]);

(iv) quasicontinuous PIC codes (code QUICKPIC from Katsouleas *et al.* [44]);

(v) centroid codes by Wang [45] and Blaskiewicz [25] (the latter also includes the effect of multipacting during the instability);

(vi) δf method for solving the Vlasov-Maxwell equations (BEST code by Qin *et al.* [46]).

An example result from a microbunch simulation for KEKB is shown in Fig. 34. Without synchrotron motion the instability affects mainly the tail particles, while with synchrotron motion the instability is weaker, but also affects the head of the bunch. Figure 35 displays the associated beam-size increase as a function of time for three different electron densities. Without synchrotron motion the beam suffers a beam breakup instability with fast emittance growth for all electron densities considered (left picture). With synchrotron motion included, a threshold electron density exists above which a fast steep growth occurs. The beam-size blowup saturates at a value well above the natural beam size. The fast instability above the threshold seems to be of the TMCI type. Below the threshold, the microbunch simulation shows a moderate emittance growth due to the classical head-tail instability, if the chromaticity is not zero (the lower two curves in the center picture). This conventional head-tail instability is not observed in some of the other simulations, such as the PIC codes. For zero chromaticity and below the TMCI threshold there seems to be yet another, slower growth (the right picture), whose origin is unexplained and which may not correspond to a slow emittance growth and beam-

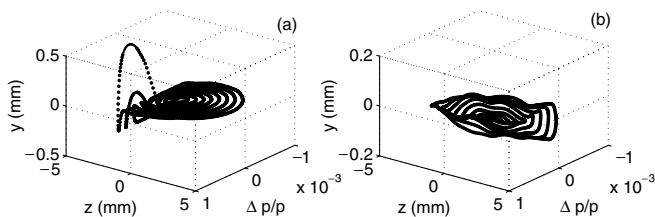


FIG. 34. Bunch shape deformation due to the interaction with electron cloud without (left) and with synchrotron motion (right) obtained from a microbunch simulation for KEKB [28]; positions of microbunches are plotted after 100 turns for an electron density of 10^{12} m^{-3} ; the synchrotron tune for the right case is $Q_s = 0.015$.

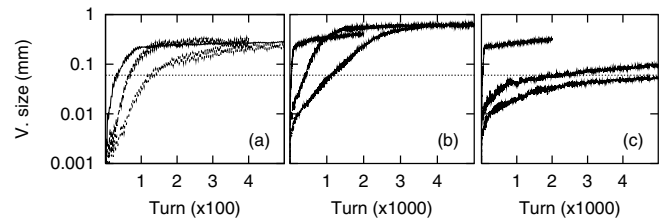


FIG. 35. Growth of the vertical rms amplitude of the microbunches without synchrotron motion (left), with synchrotron motion and chromaticity $Q'_{x,y} \approx (4, 8)$ (center), and for zero chromaticity (right) [28]; the three curves refer to electron densities of 2×10^{11} , 4×10^{11} , and 10^{12} m^{-3} ; the growth is faster for higher density; the dashed line indicates the natural rms beam size.

size blowup seen in other simulations [29] or detected at KEKB below the TMCI threshold (see Fig. 13).

Figure 36 shows the result of a microbunch simulation for PEP-II [40]. Here the instability was simulated for various bunches along a train, each of which encounters a different electron density, that increases towards an asymptotic value. The simulation reveals a 30% beam-size blowup along the train, though the asymptotic density is well below the TMCI threshold. The beam size increase is roughly consistent with observations at KEKB and PEP-II. However, the simulated beam size increase is mainly in the vertical plane. This is contrary to the actual observation at PEP-II, where the beam size blew up horizontally, but consistent with the findings at many other storage rings. Interestingly, unlike for the KEKB simulations with PEHT described above, the PEP-II simulation results from the ECI

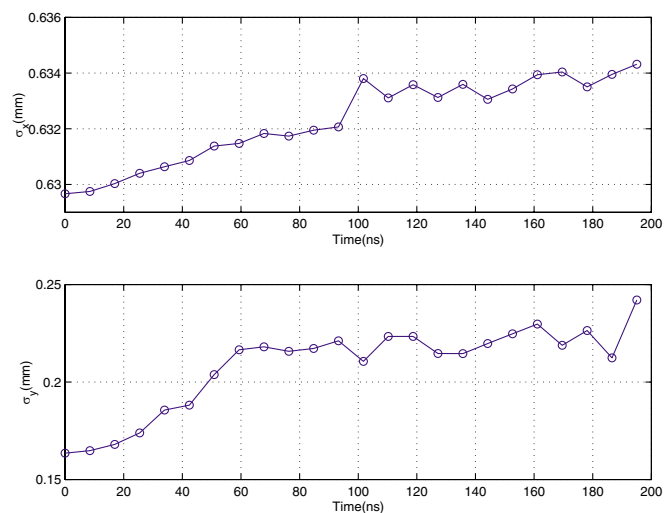


FIG. 36. (Color) Horizontal and vertical beam size increase along a PEP-II bunch train with 8.5 ns bunch spacing, simulated by a microbunch model [40]; the electron density was assumed to reach an asymptotic value of $2 \times 10^{11} \text{ m}^{-3}$ with an exponential saturation time of 50 ns; the final density is a factor 2.5 below the TMCI threshold.

code did not show any sign of the conventional head-tail instability.

The simulation scheme for the soft-Gaussian or PIC codes is illustrated in Fig. 37. As for the microbunch codes, the interaction between bunch and electrons occurs at one or several locations around the ring. However, here both beam and electrons are represented by macroparticles. The bunch macroparticles are divided into longitudinal slices, and the interaction between the beam and the cloud is computed slice by slice. The electrons move between slice centers with their instantaneous momenta and under the possible influence of external magnetic fields. After the interaction, the beam macroparticles are propagated to the next interaction point, using a 6×6 matrix representing the linear optics. Chromaticity, nonlinear fields, space charge, conventional impedances, and transverse feedback can also be included in this transformation, to study their effect on the electron-beam instability. Again as in the microbunch codes, prior to a bunch arrival the electron cloud is refreshed, i.e., the cloud is assumed to be newly generated by preceding bunches and not to keep any memory of previous perturbations. The interaction between bunch particles and cloud electrons is expressed by the following coupled equations of motion (this is the general form in the case when the kick approximation is applied and the cloud is lumped at N_{int} locations s_n around the ring) [47]:

$$\frac{d^2 \vec{x}_{p,i}(s)}{ds^2} = -\mathbf{K}(s) \vec{x}_{p,i}(s) + \frac{e}{\gamma m_p c^2} \times \sum_{n=0}^{N_{\text{int}}-1} \vec{E}_e[\vec{x}_{p,i}; f_{e,n}(x, y, t)] \delta(s - s_n), \quad (1)$$

$$\frac{d^2 \vec{x}_{e,j}(s)}{dt^2} = -\left(\frac{e}{m_e}\right) \left(\vec{E}_p[\vec{x}_{e,j}; f_{p,SL}(x, y)] + \frac{d\vec{x}_{e,j}}{dt} \times \vec{B}_{\text{ext}} \right). \quad (2)$$

Here, the positions of electrons and bunch particles are represented by the two-dimensional and three-dimensional vectors $\vec{x}_e \equiv (x_e, y_e)$ and $\vec{x}_p(s) \equiv (x_p, y_p, z_p)$, where $z =$

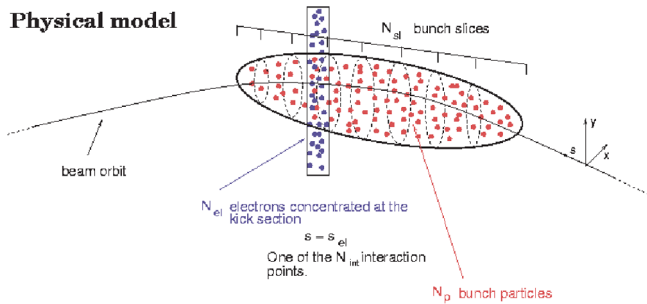


FIG. 37. (Color) Schematic of the simulation algorithm in the code HEADTAIL modeling the single-bunch instability due to an electron cloud [105].

$s - ct$ denotes a comoving longitudinal coordinate; \mathbf{K}_s is the distributed 3D focusing strength between two interaction points—commonly the effect of this focusing is integrated and compressed into a 6×6 matrix; $f_{e,n}(x, y)$ and $f_{p,SL}(x, y)$ represent the distribution functions of the electron cloud at location n and the bunch particles within a slice, respectively; \vec{E}_e is the electric field of the electrons and \vec{E}_p that of the beam, respectively; \vec{B}_{ext} is an external magnetic field that can significantly influence the electron dynamics. In the PIC approach, the electric fields $\vec{E}_{e,p}$ acting on the electrons and beam particles during their interaction are calculated on a grid. In the soft-Gaussian approximation the beam is assumed to be of locally Gaussian transverse shape with centroid position and local rms size determined from the macroparticle beam distribution within a slice, and the field of the electrons is computed from the Bassetti-Erskine expression for a non-round charge distribution [48] by assigning to the macroelectrons a small Gaussian size, typically a tenth of the rms beam size. In either case, the fields may be chosen to obey conducting boundary conditions on the chamber wall, or to have open boundaries. Results of the soft-Gaussian approximation and a PIC simulation were compared in [41].

Figures 38 and 39 present the results of PIC simulations with the code PEHTS [42] for the LHC. The two pictures refer to different electron-cloud densities; the various curves correspond to different synchrotron tune. It can be seen that for moderate electron densities a fast TMCI instability starts after a short initial lee time. The instability is suppressed, if the synchrotron tune is large enough. For the 2 times larger density in Fig. 39, the stabilizing synchrotron tune is also 2 times higher than in Fig. 38. Indeed, the TMCI instability exhibits a nearly perfect scaling with the ratio ρ_e/Q_s , as is illustrated in Fig. 40, where results for many different densities and synchrotron tunes, but con-

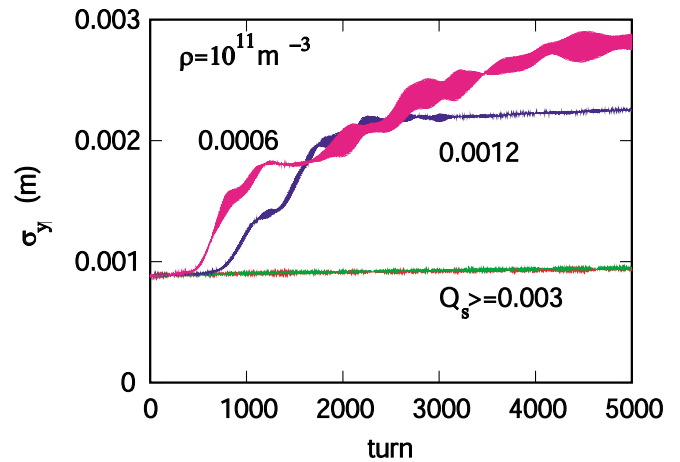


FIG. 38. (Color) Evolution of the LHC vertical beam size at injection with turn number simulated by the code PEHTS for an electron density of $1 \times 10^{11} \text{ m}^{-3}$ [88]; the curves correspond to different synchrotron tunes as indicated.

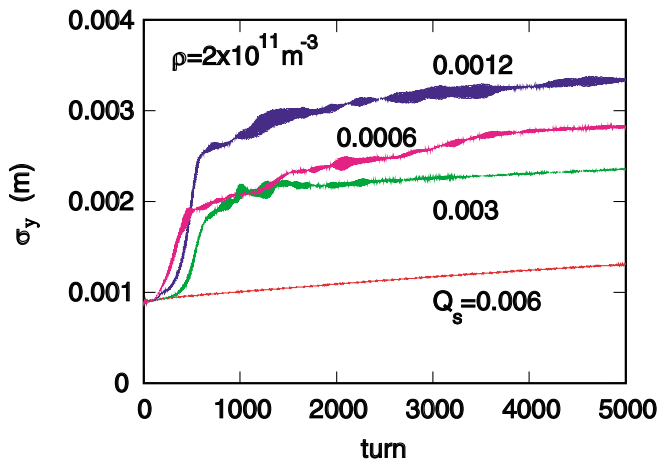


FIG. 39. (Color) Evolution of the LHC vertical beam size at injection with turn number simulated by the code PEHTS for an electron density of $2 \times 10^{11} \text{ m}^{-3}$ [88]; the curves correspond to different synchrotron tunes as indicated.

stant scaling ratio, are superimposed and the horizontal axis is weighted with the electron density. The simulated curves and the initial instability rise times coincide for all densities, as long as the latter are smaller than $5 \times 10^{11} \text{ m}^{-3}$. For higher densities, another type of blowup occurs, which starts directly at time zero and which resembles an incoherent effect.

For the purpose of benchmarking, several comparisons were performed between the two PIC codes PEHTS and HEADTAIL. Figures 41 and 42 show, as an example, the simulated suppression of the beam-size blowup by a positive chromaticity in KEKB simulated by the two codes for an electron density of 10^{12} m^{-3} and one electron-beam interaction per turn. Note that the horizontal scale in Fig. 41 is about twice that in Fig. 42 (one turn is about

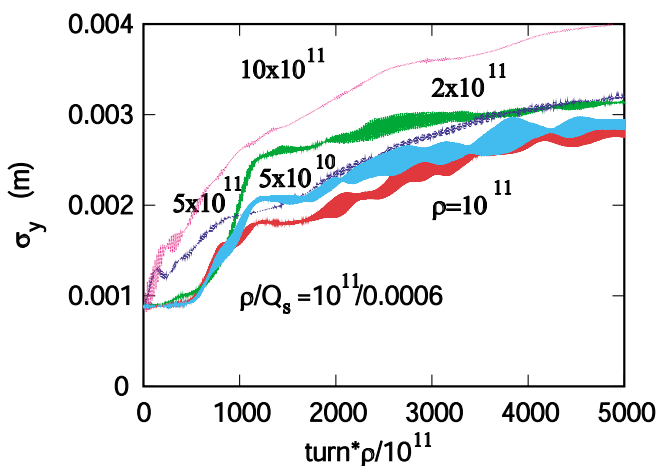


FIG. 40. (Color) Evolution of the LHC vertical beam size at injection versus normalized product of turn number and electron density, simulated by PEHTS, for various densities and synchrotron tunes, keeping their ratio constant [88].

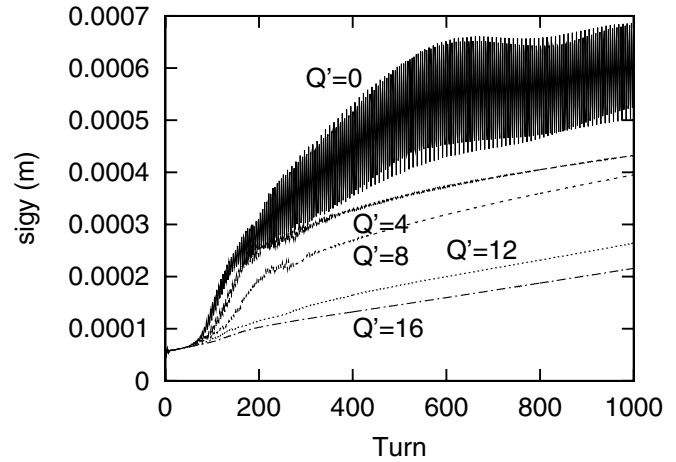


FIG. 41. Vertical rms beam-size growth of a KEKB bunch over 1000 turns for different values of chromaticity Q_y , simulated by the PEHTS code [42,85].

$10 \mu\text{s}$). The agreement between the two codes is quite satisfactory. Both predict that the instability can be cured by increasing the chromaticity. Neither suggests the occurrence of a conventional head-tail instability, but both show a persistent gradual growth in the beam size, even when the fast instability is suppressed. These simulations did not include radiation damping. The KEKB LER transverse radiation damping time is about 46 ms or 4600 turns, thus 5–10 times longer than the time scales considered in Figs. 41 and 42. Actual beam-size increase below the TMCI threshold is, therefore, likely, and might be consistent with the observations, e.g., in Fig. 13.

In order to investigate whether HEADTAIL or PEHTS yield realistic results and if no important physics is missing, in late 2001 a collaboration was launched between CERN and the University of Southern California (USC) to upgrade the plasma code QUICKPIC developed at UCLA and USC for

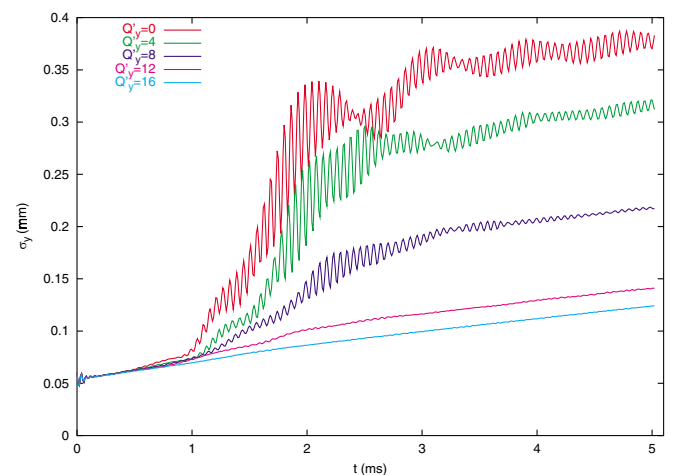


FIG. 42. (Color) Vertical rms beam-size growth of a KEKB bunch over 500 turns for different values of chromaticity Q_y simulated by the HEADTAIL code [85].

modeling the electron-cloud instability in a large storage ring. QUICKPIC had been written to simulate plasma wake-field acceleration in a few-meter long plasma [49]. The code was extensively benchmarked against a more elaborate code OSIRIS and against experimental results obtained in the SLAC FFTB beam line (see, e.g., [50]). The advantages of the QUICKPIC benchmarking are (1) the code was validated with controlled experimental data, and (2) it does not consider one or few electron-beam interaction points per turn, but it models the continuous beam-electron interaction around the ring, employing a “quasistatic” or “-frozen-field” approximation [49,51,52], where the wake is assumed to depend only on $z = s - ct$ and to remain constant for a fraction, i.e., $1/30$, of a betatron wavelength [44]. This approximation makes it much faster than OSIRIS. It was thought to be necessary for simulating the evolution of the beam over many tens of kilometers. The quasistatic approximation is valid as long as $\beta \gg \sigma_z$. It implies that only 2D Poisson equations need to be solved rather than 3D equations as in OSIRIS. QUICKPIC simulations include all magnetic and electric fields of the electrons and the beam. In order to model the electron cloud, some extensions of the original code were required. For example background ions had to be removed and also the beam transverse and longitudinal motion to be added [44]. After these modifications, the treatment in QUICKPIC can be considered as rather similar to those in the PEHTS and HEADTAIL codes, the main differences being, as already indicated, the inclusion of all magnetic fields and a much larger number of electron-cloud wakefield “kicks,” which in QUICKPIC are applied quasicontinually around the ring, rather than at a few locations. Figure 43 presents a typical QUICKPIC result. Shown are initial density profiles of the electrons and the beam, prior to the development of an instability.

In 2002, a wider interlaboratory comparison of electron-cloud buildup and instability-simulation codes was initiated. The contact persons identified at the time are Blaskiewicz (BNL), Cai (SLAC), Furman (LBNL), Katsouleas (USC), Ohmi (KEK), Pivi (then LBNL, now SLAC), Wang (then KEK, now BNL), Qin (PPPL), Rumolo (then CERN, now GSI), Wang (LANL), and

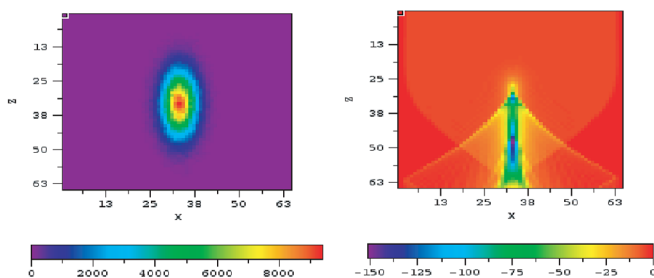


FIG. 43. (Color) Initial beam (left) and electron density (right) in the $x - z$ plane, at $y = 0$, simulated by QUICKPIC for the CERN SPS; the electron peak density enhancement by a factor 150 is reached $1.9\sigma_z$ behind the bunch center [44].

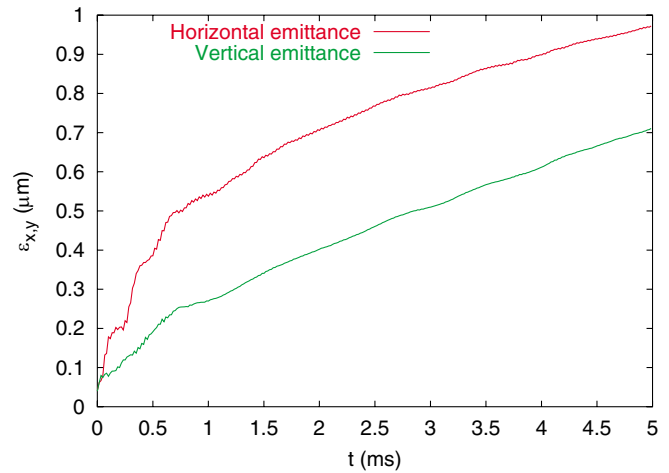


FIG. 44. (Color) HEADTAIL simulation result by Rumolo of horizontal and vertical emittance growth for the code benchmarking with the parameters of Table I; the horizontal scale extends over 5 ms, the vertical from 0 to $1 \mu\text{m}$; one beam-electron interaction per turn was considered.

Zimmermann (CERN), to which one should add Bellodi (RAL), who has made outstanding contributions. For the buildup simulations the code comparison was fairly successful. Results were obtained from the codes CSEC (Blaskiewicz), E-CLOUD (Rumolo and Zimmermann), PEI (Ohmi), POSINST (Pivi and Furman), and CLOUDLAND (Wang). The comparison was less successful for the instability simulations, where only three results are available, namely, from HEADTAIL, PEHTS, and QUICKPIC. Further details and updated information on the code comparison, including all of the benchmarking parameters, can be found on the comparison web page <http://wwwslap.cern.ch/collective/ecloud02/ecsims>.

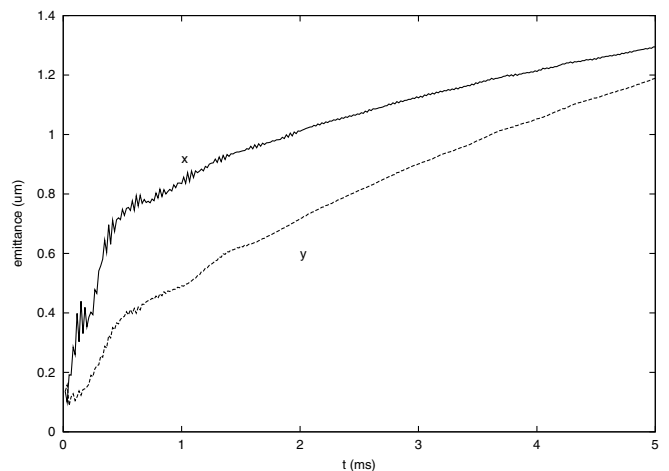


FIG. 45. PEHTS simulation result by Ohmi of horizontal and vertical emittance growth for the code benchmarking with the parameters of Table I; the horizontal scale extends over 5 ms, the vertical from 0 to $1.4 \mu\text{m}$; one beam-electron interaction per turn was considered.

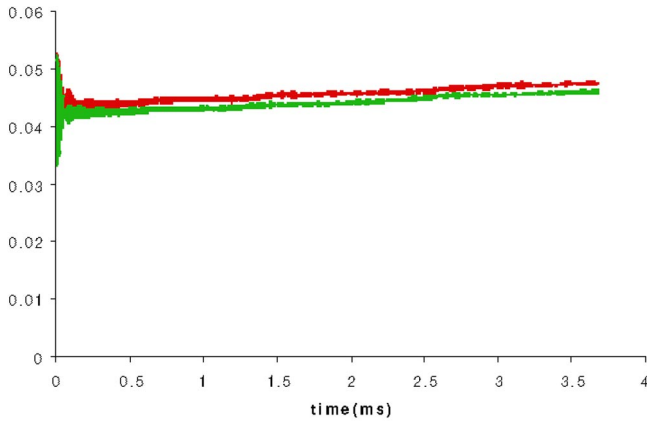


FIG. 46. (Color) QUICKPIC simulation result by Ghalam and Katsouleas of horizontal and vertical emittance growth for the code benchmarking with the parameters of Table I; the horizontal scale extends over 4 ms, the vertical from 0 to $0.06 \mu\text{m}$; a continuous electron-beam interaction was modeled.

Figures 44–46 present some results of the code comparison for the benchmarking parameters listed on the web site and reproduced in Table I, which approximately correspond to the CERN SPS. HEADTAIL and PEHTS give nearly identical results, namely, a large emittance growth by more than a factor of 10 in both planes, whereas in QUICKPIC the emittance growth is only a few percent, perhaps consistent with zero. The main difference between the simulations is that in HEADTAIL and PEHTS a single interaction point per turn was considered, while QUICKPIC models a quasicontinuous interaction (the lattice was

TABLE I. Parameters for benchmarking of instability simulation codes.

Variable	Symbol	Value
Bunch population	N_b	1×10^{11}
Electron density	ρ_e	10^{12} m^{-3}
Round chamber radius	b	2 cm
Focusing		Smooth
Beta function	$\beta_{x,y}$	100 m
Chromaticity	Q'	0
Energy spread	δ_{rms}	0
Synchrotron motion		None
Beam energy	E_b	20 GeV
Ring circumference	C	5 km
Betatron tunes	$Q_{x,y}$	26.19, 26.24
Bunch profile		Gaussian
rms bunch length	σ_z	30 cm
rms transverse size	$\sigma_{x,y}$	2 mm
Magnetic field	B	None
Electric boundary		Conducting or open
No. of beam-electron interactions/turn	n_{IP}	1 or several
Boundary for electrons		Elastic reflection on wall

treated in a smooth approximation with constant beta function). Another difference is that QUICKPIC assumed conducting boundaries, and the two other codes open boundaries. For the case considered, no fast TMC-like instability occurs in any of the simulations. We might expect a better agreement between codes, when such instability is present.

A second attempt was later made, by Benedetto and Ghalam, to benchmark the program HEADTAIL against QUICKPIC. In this case, conducting boundaries for rectangular boundaries were employed in both codes. In addition, QUICKPIC was modified, for the purpose of this comparison, to model a single discrete interaction point instead of a continuous interaction. Example parameters for the LHC were considered here. The results of both codes for the horizontal and vertical plane are displayed in Figs. 47 and 48, respectively. The agreement is considerably improved compared with the previous example, but a factor of 2 discrepancy in the emittance growth still remains. Its origin is uncertain, since the physics in these two simulations is now thought to be essentially identical.

Returning to the original large difference between the continuous QUICKPIC and the discrete HEADTAIL, Fig. 49 illustrates that the character of the simulated emittance growth can indeed change as the number of beam-electron interaction points per turn is increased. For a small number the emittance growth starts at time zero and has an incoherent flavor, while for a number equal to or larger than 5, the initial emittance growth is small and the TMCI-like instability becomes noticeable after about 20 ms.

A further aspect worth mentioning is the sensitivity of the electron-cloud effect to other additional perturbations, such as conventional impedance or space charge. Figures 50 and 51 show by now classical simulation results of electron-cloud induced blowup in the SPS, whether or

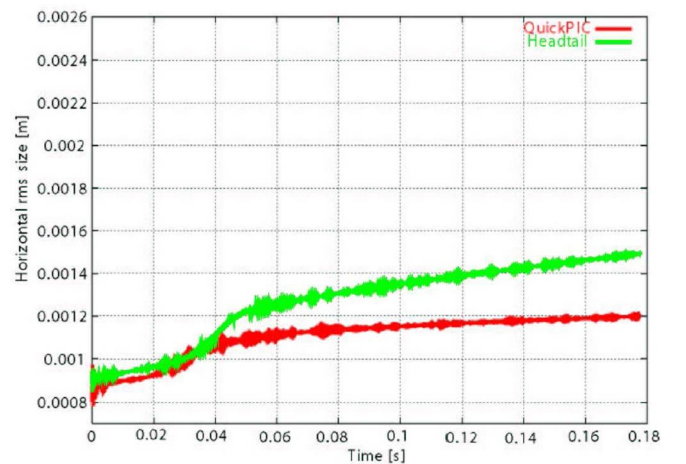


FIG. 47. (Color) Horizontal emittance growth for LHC example parameters as a function of time simulated by HEADTAIL (green curve) and by the discretized QUICKPIC (red curve) with a single electron-beam interaction per turn.

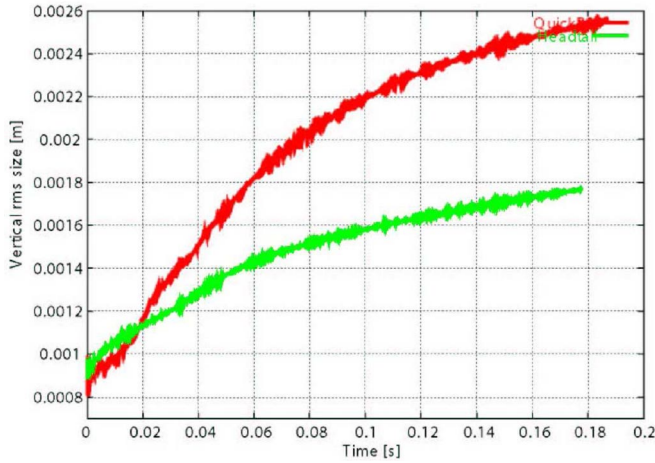


FIG. 48. (Color) Vertical emittance growth for LHC example parameters as a function of time simulated by HEADTAIL (green curve) and by the discrete version of QUICKPIC (red curve) with a single electron-beam interaction per turn.

not space charge is included [53]. In this case, without space charge, the electron cloud leads to a monotonic blowup in the beam size, and to almost no dipolar motion of the slice centroids. When space charge is added to the electron cloud, the character of the instability changes and a violent head-tail motion ensues. We note that in this example the coherent tune shift from the electron cloud [54] is about 0.0077 (the incoherent tune shift is much larger due to the electron pinch during the bunch passage), while the space-charge tune shift at the center of the bunch is -0.0365 .

Figure 52 shows a simulation of the combined effect of electron cloud and broadband impedance (the coherent tune shifts resulting from these two sources are of similar

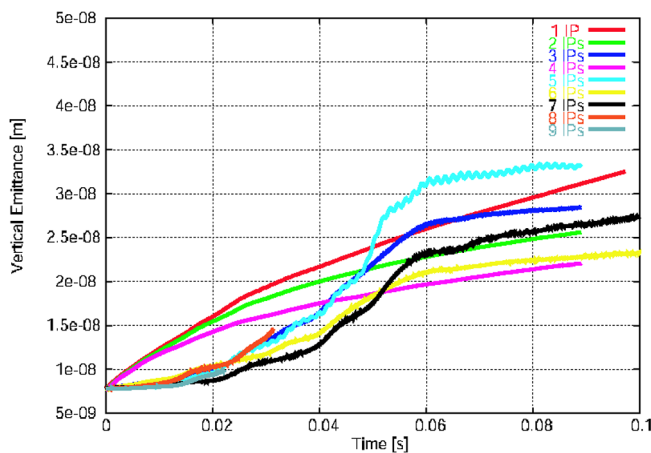


FIG. 49. (Color) Vertical emittance growth in the LHC at injection as a function of time, simulated by HEADTAIL, for various numbers of beam-electron interaction points (the various curves), increasing from 1 to 9 in steps of 1; the cloud density is $6 \times 10^{11} \text{ m}^{-3}$ [29].

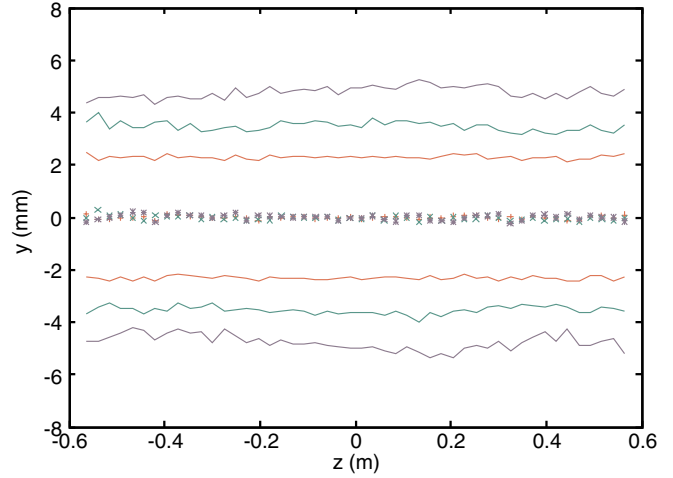


FIG. 50. (Color) Simulated vertical bunch shape (centroid and rms beam size) after 0, 250, and 500 turns in the CERN SPS assuming a cloud density of 10^{12} m^{-3} without proton space charge [53]; the HEADTAIL code was used; the vertical scale extends from -8 to $+8$ mm, the horizontal axis from -0.6 to $+0.6$ m ($\pm 2\sigma_z$).

order of magnitude in the SPS), as well as the combined effect of broadband impedance and space-charge tune spread, and the effect of the broadband impedance alone. It is evident that the electron cloud greatly modifies the effect of the broadband impedance and renders the beam more unstable.

Figure 53 illustrates the effect of a positive chromaticity on the beam-size blowup by for the SPS. The suppression of the instability by a chromaticity of $Q'_y \approx 10$ is roughly consistent with observations. In Figs. 41 and 42 we pre-

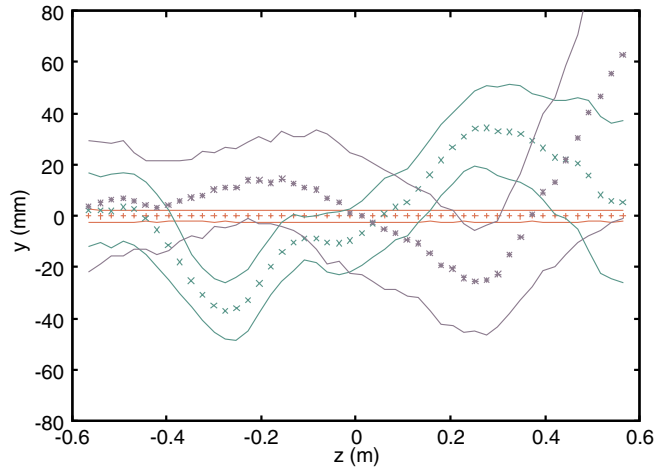


FIG. 51. (Color) Simulated vertical bunch shape (centroid and rms beam size) after 0, 250, and 500 turns in the CERN SPS assuming a cloud density of 10^{12} m^{-3} with proton space charge at $26 \text{ GeV}/c$ [53]; the HEADTAIL code was used; the vertical scale extends from -8 to $+8$ mm, the horizontal axis from -0.6 to $+0.6$ m ($\pm 2\sigma_z$).

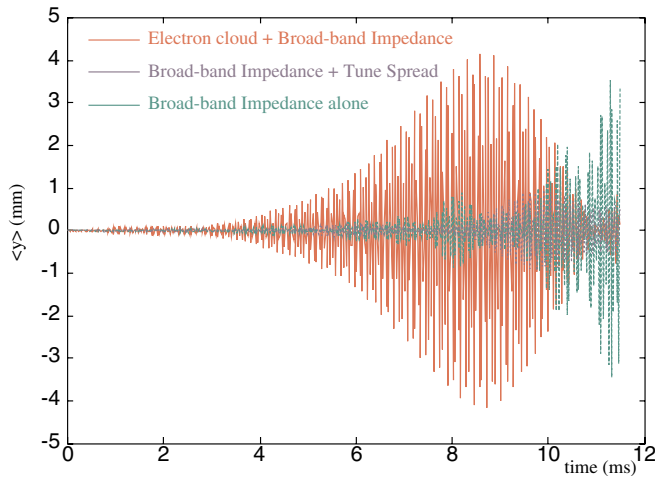


FIG. 52. (Color) Evolution of the centroid vertical position of an SPS bunch over 500 turns considering the combined effect of electron cloud and broadband impedance (red), the effect of broadband impedance and an additional space-charge tune spread (blue), and the broadband impedance alone (green) [41]; the simulation was performed with HEADTAIL.

sented similar simulations for KEKB. A difference is that, for the SPS, in order to obtain the remedial action of the chromaticity it was necessary to include the effect of a broadband resonator; for completeness space charge was also taken into account. Without the broadband resonator, the positive chromaticity has no positive effect for the SPS, which is different from the KEKB case. This result underlines the importance of such synergistic components.

Before concluding the discussion of simulations, we take a look at electron-cloud effects in single-pass systems.

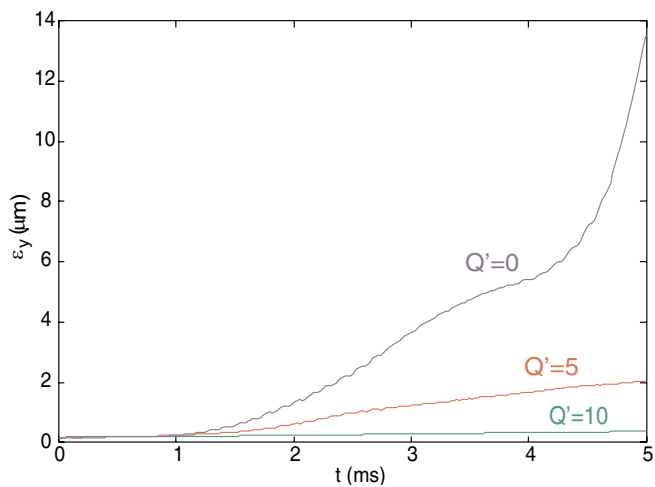


FIG. 53. (Color) Simulated vertical emittance of an SPS bunch at injection as a function of time over 5 ms for three different values of the vertical chromaticity; a broadband resonator impedance and space charge are included in addition to the electron cloud [85]; the simulation was performed with the HEADTAIL code.

As a critical example, we consider the beam delivery system of a future linear collider, which is particularly vulnerable to electron-cloud effects, since it must produce an unprecedented small spot size at the electron-positron interaction point (IP), which implies tight tolerances on emittance preservation and optics control. A study has recently been performed for the NLC beam delivery by Chen *et al.* [55], where an electron cloud can build up during the passage of a positron bunch train. For sufficiently high secondary emission yields, the electron cloud may reach densities up to 10^{14} m^{-3} . The study [55] demonstrated that the IP spot size is significantly degraded, if the electron cloud density exceeds a critical value of about 10^{11} m^{-3} , as is illustrated by simulation results from the “CLOUD_MAD” program [56] in Fig. 54.

In the beam-delivery system of an electron-positron linear collider, two effects of the electron cloud could cause a blow up of the IP spot size: the breakdown of the so-called “ $-I$ ” transform between chromatic-correction sextupoles and the direct focusing effect. The breakdown of the $-I$ occurs due to the change in phase advance induced by the additional focusing:

$$\Delta\phi \approx \frac{2\pi r_e \rho_e \langle \beta \rangle L}{\gamma}, \tag{3}$$

with L denoting the distance between the two sextupoles, ρ_e the electron volume density, $\langle \beta \rangle$ the average beta function, and r_e the classical electron radius. The direct focusing effect leads to a relative increase in the IP spot size, which can be estimated by

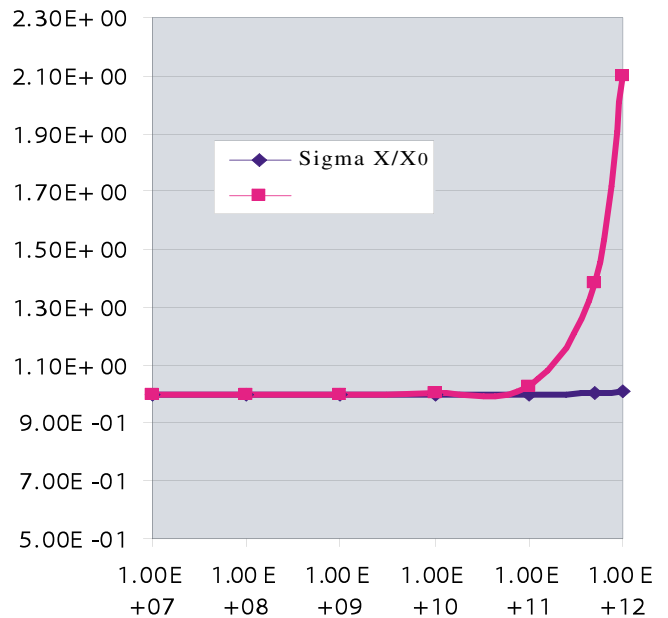


FIG. 54. (Color) Relative vertical (pink) and horizontal (blue) IP beam-size increase as a function of the electron cloud density, as simulated by CLOUD_MAD [55]; the horizontal axis is logarithmic, and it extends from 10^7 to 10^{12} m^{-3} .

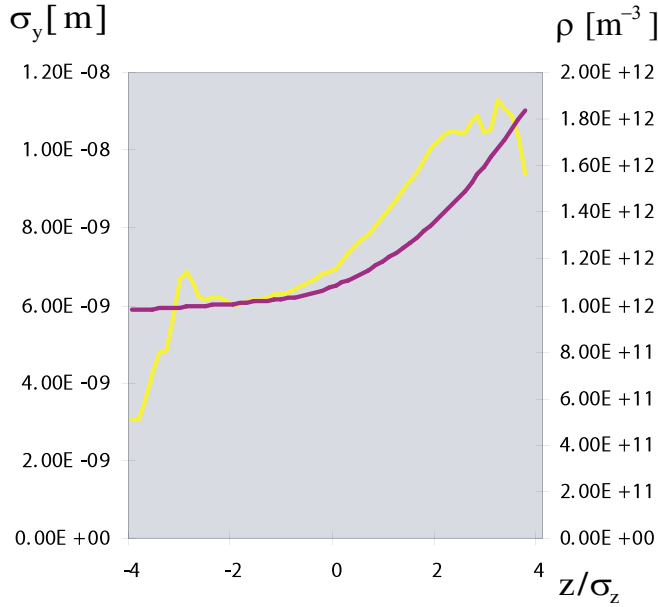


FIG. 55. (Color) Simulated vertical rms size of the positron beam in units of m (purple) and the electron density at the center of the beam 100 m upstream of the IP (yellow) as a function of the longitudinal position z/σ_z along the bunch [55]; the bunch tail is on the right.

$$\frac{\Delta\sigma_y^*}{\sigma_y^*} \approx \frac{2\pi}{\gamma} \int_0^C \rho_e \beta_y \sin^2[\phi^* - \phi(s)] ds. \quad (4)$$

In both cases the electron density ρ_e strongly depends on the longitudinal position z inside the bunch, which implies that different longitudinal slices of the bunch are affected differently.

Detailed studies have proven that the direct focusing contribution is the dominant effect for the NLC [55]. Figure 55 shows that at the IP the tail of the bunch is blown up, as expected for beam breakup without synchrotron motion and that the shape of the blowup resembles the pinch of the electron cloud during the bunch passage monitored at an upstream location with large beta function.

IV. ANALYTICAL TREATMENTS

Analytical models for the beam-electron interaction provide additional insight and furnish scaling laws. They also can be used as independent benchmarks for the simulations. Conversely, the latter allow for the numerical verification of analytical approximations. An important aspect of the electron-cloud response to the passing beam is their accumulation near the beam center, which is sometimes called the “electron pinch.” The pinched electrons, whose density increases during the bunch passage, introduce a tune spread, nonlinear fields, and a dynamic variation of the beta function with longitudinal and radial position. Experimental evidence for an electron-cloud induced beta beating was presented at the ELOUD’04

workshop [57]. With a brief delay, the pinched electrons follow any transverse-longitudinal perturbation of the beam distribution, e.g., a head-tail tilt. The effect of this additional transverse electron motion during the bunch passage, which is induced by a beam perturbation, can be interpreted as an effective head-tail “wakefield.” This “-electron-cloud wake” depends on many parameters, for instance, the bunch intensity, the magnetic field, the chamber dimensions, and the, e.g., conducting, boundary conditions [44]. The net cloud response to a perturbation in the beam can drive instabilities. Depending on the cloud density, the instability could appear as a beam breakup with a rise time much shorter than the synchrotron period ($\tau \ll T_s$), as a transverse mode coupling instability with a rise time comparable to the synchrotron period ($\tau \approx T_s$), or as a conventional head-tail instability, which typically has a slower growth rate ($\tau \gg T_s$). It has further been speculated whether a more “exotic monopole” instability could be driven by the electron cloud as well [52]. In addition, electron-induced tune spread and resonance excitation can conceivably cause an incoherent emittance growth, which might explain the results of some as yet unexplained simulations and measurements.

The electron-cloud buildup saturates when the electron losses balance the electron generation rate. This can happen either, at low bunch charges, when the average neutralization density is reached [58] or, at high bunch currents, when the electron kinetic energy at the moment of emission from the wall is too low to penetrate into the space-charge field of the cloud [59]. The estimates for the equilibrium electron volume density are

$$\rho_{e,\text{sat}} \approx \frac{N_b}{\pi s_b b^2} \quad \text{for } N_b \ll N_{\text{trans}} \quad (5)$$

and

$$\rho_{e,\text{sat}} \approx \frac{E_s}{m_e c^2 b^2 r_e} \quad \text{for } N_b \gg N_{\text{trans}}, \quad (6)$$

where b denotes the chamber radius (for simplicity we consider a round chamber), s_b the bunch spacing, E_s the average energy of the emitted secondary electrons, and r_e the classical electron radius. The transition occurs at a bunch population of about [60]

$$N_{\text{trans}} \approx \frac{E_s s_b}{m_e c^2 r_e}. \quad (7)$$

Therefore, if multipacting occurs, the average electron density in the steady state first increases linearly with current, until it reaches the transition intensity N_{trans} , above which the average density stays approximately constant, while the density at the center of the chamber decreases [59], reducing the strength of electron-driven instabilities above the transition intensity.

The effective electron-cloud wakefield is proportional to the electron-cloud density and the ring circumference. The

magnitude of both single-bunch and coupled-bunch wakes can be estimated as [28,61]

$$W_0 \approx (4 \dots 8) \frac{\pi \rho_e C}{N_b}, \quad (8)$$

where the larger coefficient corresponds to the single-bunch wake. Here, it is assumed that the electrons perform at least a quarter oscillation in the bunch potential.

The electron cloud induces a coherent single-bunch tune shift which is related to the initial electron density, prior to the bunch passage, via [54]

$$\Delta Q \approx \frac{r_p}{2\gamma} \langle \beta \rangle \rho_e C, \quad (9)$$

where r_p denotes the classical radius of the beam particles, e.g., of protons or positrons. For a flat beam and a flat geometry the vertical tune shift could be larger by a factor of 2.

Various analytical estimates are also available for instability growth rates and thresholds. The first estimate [62] adapted the theory of the fast beam-ion instability [63] to the single-bunch electron-cloud blowup, taking into account that—unlike the creation of ions during the passage of a bunch train experiencing the fast beam-ion instability—the electrons of the cloud are produced by the preceding bunches or bunch passages and are already present prior to the bunch arrival. The estimate which describes the rise time of the single-bunch beam breakup induced by the electron cloud is (here for a positron beam) [62]

$$\frac{1}{\tau} \approx 4\pi c r_e^{3/2} \frac{\rho_e N_b^{1/2} \sigma_z^{1/2} \langle \beta \rangle}{\gamma \sigma_x^{1/2} \sigma_y^{1/2}}. \quad (10)$$

In Ref. [28] a different model of two particles was employed to describe single-bunch instabilities driven by the electron cloud. For a conventional impedance, such simplified models typically employ pointlike particles. However, in the case of the electron cloud, the oscillation of the electrons in the bunch potential is important. Therefore, we must assign a length at least to the driving particle. The resulting expression for the beam breakup (BBU) growth rate is (for a flat positron beam) [28]

$$\frac{1}{\tau_{\text{BBU}}} \approx \begin{cases} 2\pi r_e c \rho_e \langle \beta \rangle / \gamma & \text{for } \sigma_z \omega_e > c\pi/2 \\ \pi r_e^2 c \rho_e N_b \sigma_z \langle \beta \rangle / (\gamma \sigma_x \sigma_y) & \text{for } \sigma_z \omega_e < c\pi/2, \end{cases} \quad (11)$$

where ω_e denotes the single-electron, e.g., vertical, angular oscillation frequency inside the bunch:

$$\omega_e = c \left(\frac{2N_b r_e}{\sigma_y (\sigma_x + \sigma_y) \sqrt{2\pi} \sigma_z} \right)^{1/2}. \quad (12)$$

The expression for the growth rate τ_{BBU} depends on whether the electrons perform at least one quarter oscillation over the rms bunch length or not, and, accordingly, is either independent of the bunch length or linearly increas-

ing. By contrast, the previous expression (10), based on a model of the continuous two-stream interaction, depends on the square root of the bunch length.

With synchrotron motion, at low electron density the beam breakup is suppressed. In this case, the same two-particle model can be used to estimate the growth rate of the conventional head-tail instability, e.g., considering again the high-frequency long-bunch case of (11) for the $l = 1$ head-tail mode one finds (for positrons, whose slip-page factor η is approximately equal to the momentum compaction factor α_C) [28]

$$\frac{1}{\tau^{(1)}} \approx \frac{64}{3} r_e \frac{\rho_e \langle \beta \rangle \sigma_z Q'_y}{T_0 \alpha_C \gamma}, \quad (13)$$

which increases linearly with chromaticity, bunch length, and cloud density.

At higher electron density, the threshold of the transverse mode coupling instability may be reached. In the case of the electron cloud, this threshold is a threshold in the electron density (rather than in the beam intensity), which takes the simple form [28]

$$\rho_{\text{thr}} \approx \frac{2}{r_e c} \frac{\gamma Q_s}{T_0 \langle \beta \rangle}, \quad (14)$$

where Q_s is the synchrotron tune.

Another approach is to establish and exploit some correspondence between the electron-cloud wake and a conventional wake. Simulations for a constant beam line density suggested that the electron-cloud Green-function wake (i.e., the wake excited by a single displaced slice) is fairly well parametrized by a damped broadband resonator of the form [64]

$$W(z) \approx -c \frac{R_s}{Q_R} \frac{1}{\sqrt{1 - 1/(4Q_R^2)}} \exp\left(-\frac{\omega_R z}{2cQ_R}\right) \sin\left(\frac{\omega_R}{c} z\right). \quad (15)$$

The three free parameters are the resonator frequency ω_R , the quality factor Q_R , and the shunt impedance R_s . The resonator frequency is roughly equal to the linear electron oscillation frequency at the center of the bunch

$$\omega_R \approx \omega_e = c \left(\frac{2N_b r_e}{\sigma_y (\sigma_x + \sigma_y) \sqrt{2\pi} \sigma_z} \right)^{1/2}. \quad (16)$$

The shunt impedance can be obtained analytically considering an initial cloud of Gaussian transverse shape and of the same size as the beam, with the result, for the vertical plane, [64]

$$\frac{cR_s}{Q} = H_{\text{enh}} \frac{2^{5/4} \pi^{5/4} \rho_e \sigma_x r_e^{1/2} \sigma_z^{1/2} C}{(\sigma_x + \sigma_y)^{3/2} \sigma_y^{1/2} N_b^{1/2}}, \quad (17)$$

where an additional empirical factor H_{enh} was introduced to represent the contribution from electrons at larger amplitudes. In simulations of wakefields for the SPS and

KEKB, the factor H_{enh} was found to be 3–4 vertically and 7–20 horizontally. This factor can also be estimated analytically, e.g., at the end of the bunch passage, as [44,65]

$$H_{\text{enh}} \approx \left(1 + \frac{2\omega_{R,x}\sigma_z}{\sqrt{\pi}}\right) \left(1 + \frac{2\omega_{R,y}\sigma_z}{\sqrt{\pi}}\right), \quad (18)$$

where the number of linear electron oscillations along the bunch was taken to be equal to $2\sqrt{\pi}\omega_R\sigma_z/(2\pi)$.

The effective quality factor is low, $Q_R \approx 1$. It reflects a damping that arises from the nonlinear force acting between the beam and the electrons as well as from the frequency spread due to the variation of the beta functions around the ring and due to the longitudinal variation of the beam line density along the bunch. Once the wakefield is approximated by a broadband resonator, a standard stability analysis can be applied. For example, invoking the conventional formula from Zotter [66], the TMCI threshold intensity for long bunches and zero chromaticity becomes [67]

$$N_{n,\text{thr}} \approx 5.3 \left(\frac{\omega_R\sigma_z}{c}\right)^2 \frac{Q_R\gamma Q_s}{cR_e\langle\beta\rangle(R_s/Q_R)} \quad \text{for } \omega_R\sigma_z \gg c. \quad (19)$$

In the case of the electron cloud, this is an implicit equation for the threshold intensity, since on the right-hand side ω_R and R_s/Q_R depend on $N_{b,\text{thr}}$.

One can also compute a threshold for the ‘‘fast blowup’’ which was studied for a conventional impedance by Ruth and Wang [68], Pestrikov [69], and Kernel *et al.* [70]. Applying this theory to the electron-cloud instability [64], and considering an arbitrary chromaticity Q' , the corresponding threshold is [64]

$$N_{b,\text{thr}} \approx \frac{4\pi C}{e^2 c^3 Z_0} \frac{4\eta(\Delta p/p)_{\text{rms}}|\omega_R + \omega_\xi|E\sigma_z}{\langle\beta\rangle|\text{Re}(Z_{\text{eff}}(\omega_{\text{max}}))|}, \quad (20)$$

where $(\Delta p/p)_{\text{rms}}$ denotes the rms momentum spread, Z_0 the vacuum impedance, $\omega_\xi = Q'c/(\eta C)$ the chromatic frequency shift, and $\omega_{\text{max}} \approx \omega_R$ the frequency at which the real part of the impedance assumes a maximum. Again, this is an implicit equation.

Alternatively, if the electrons perform many oscillations inside the bunch, we can invoke a coasting beam approximation. Using formulas of Refs. [34,71–73] one then finds the threshold condition

$$\left(\frac{\sqrt{3}r_p c^2}{4T_0\omega_\beta\sqrt{\pi\ln 2}}\right) \frac{N_b}{\gamma} \frac{cR_s}{Q_R} \frac{Q_R}{\omega_R^2} \approx \sigma_z\sigma_\delta\eta \left|1 + \frac{\xi\omega_\beta}{\eta\omega_R}\right|, \quad (21)$$

which assumes a mode number $l \approx \omega_R\sigma_z/c$ near the peak of the resistive part of the electron cloud impedance. In particular, the right-hand side is zero and there is no Landau damping at all if $\omega_R \approx -\omega_\beta\xi/\eta$ (here ω_β is the betatron frequency, including integer part, in units of s^{-1} and η the slippage factor). As for the usual bunched-beam

head-tail instability, above transition this situation is met at negative values of the chromaticity. The left-hand side of the above equation scales with intensity and bunch length as $\sigma_z^{3/2}H_{\text{enh}}\rho_e/N_b^{1/2}$, where H_{enh} is the pinch enhancement factor.

Several multiparticle models were developed to represent the combined effect of the electron cloud and the beam-beam interaction or space charge. A weak-strong approach was studied which models the electron-cloud wake and the incoherent tune shift due to the electron pinch which was assumed to linearly increase along the bunch. To this, also a quadratic tune shift around the bunch center was added, which approximates the additional incoherent focusing from beam-beam or space charge forces [74]. An underlying assumption was that the bunch needs to be represented by more than two macroparticles in order to correctly observe a destabilizing effect from the various z -dependent tune shifts, whereas a δ -dependent tune shift would require only two macroparticles to produce the conventional weak head-tail instability [75].

An alternative strong-strong model for electron cloud and (here electron-positron) beam-beam interaction represents the positron bunch by two macroparticles, and the electron beam by a single one. The macroparticles of the two beams collide on either side of, and close to, the main interaction point. The electron cloud effect is represented by a constant head-tail wakefield coupling the leading and the trailing positron macroparticle once per turn [76]. The synchrotron motion and the resulting change of the longitudinal order of the macroparticles are crucial for both the weak-strong and the strong-strong models.

An impressive variety of elaborate analytical and semi-analytical model descriptions were constructed to understand the instability of long proton bunches in the PSR and to make predictions for the future Spallation Neutron Source (SNS). In the following paragraphs, we can only give a brief summary. Interested readers are referred to the original literature for further details.

In [77], Wang and colleagues derived centroid equations for protons and electrons assuming a transversely uniform distribution (so that the forces between beam and electrons are linear) and a Lorentzian frequency distribution for both the beam and the electrons. Starting from the centroid equations, approximate solutions for the one-pass two-stream instability are obtained. The amplitude grows quasiexponentially due to the instability, while it is damped exponentially by the frequency spread; the instability growth rate is a function of both longitudinal position and time. More specifically, for a longitudinally uniform electron density and a parabolic bunch profile of total length l the amplitudes of both beam and electrons grow as [77]

$$\exp\left(-\Delta_p t + \left(\frac{\Delta_p - \Delta_e}{\nu}\right)z' + \sqrt{2\omega_\beta J(z')\left(t - \frac{z'}{\nu}\right)}\right), \quad (22)$$

where Δ_p denotes the (Lorentzian) frequency spread of the protons, Δ_e that of the electrons,

$$J(z') \approx \frac{3r_p c^2 \lambda_e}{a^2 \gamma \omega_\beta^2} \frac{\omega_e l}{\nu} \left(\frac{z'}{l}\right)^2 \left[1 - \frac{14}{9} \left(\frac{z'}{l}\right) + \frac{4}{3} \left(\frac{z'}{l}\right)^2 - \frac{8}{15} \left(\frac{z'}{l}\right)^3 \right], \quad (23)$$

ν is the beam velocity, λ_e the electron line density, a the radius of the beam and electrons, and z' is the longitudinal position in the beam frame with respect to the head of the bunch, which extends from $z' = 0$ to $z' = l$.

The above equation shows that a spread in the electron oscillation frequency introduces damping with the longitudinal position z' , but not in time t , while the proton frequency spread leads to a temporal damping.

A different approach is pursued by Channell in Ref. [78]. Based on the observation that in the linear theory the electron oscillation amplitudes are much larger than those of the protons he considers the nonlinear electron regime. For simplicity he assumes that the electron amplitudes have reached saturation and drive the proton beam at fixed oscillation amplitude. Depending on whether the saturated electron oscillation has a frequency spread or not, the secular growth of the proton amplitude is either linear or logarithmic in time. This result is reminiscent of the amplitude growth determined by Heifets for the nonlinear regime of the fast beam-ion instability [79]. An important ingredient of Channell's theory is that the coherent phase of the large-amplitude electron oscillation driving the beam motion is carried by a small oscillation at the head of the proton bunch. This suggests a possible cure [78]: Driving small oscillations of the bunch head by an external excitation at a frequency different from the betatron frequency would destroy the phase coherence from turn to turn, which might suppress the instability.

Blaskiewicz [80] includes the proton space charge, which in his studies is the dominant effect. Considering a square-well approximation for the rf and a longitudinal boxcar beam distribution he reduces the dimensionality of the eigenvalue problem and can solve the dispersion relation in the presence of linear space charge and electron cloud. After adding nonlinear space charge, i.e., an amplitude-dependent tune shift, and treating it as in [81], the threshold is seen to be a strong function of the electron survival during the gap. Small changes in the residual electron line density might then explain the insensitivity of threshold intensity to bunch length which is observed in the PSR (where, for fixed bunch length, the measured threshold rf voltage scales linearly with the intensity; see Fig. 9) [80].

Qin and co-workers developed a 3D self-consistent description of the two-stream instability starting from the nonlinear Vlasov-Maxwell equations in the electrostatic and magnetostatic approximation [46,82]:

$$\left\{ \frac{\partial}{\partial t} + \vec{v} \cdot \frac{\partial}{\partial \vec{x}} + \vec{F}_j \cdot \frac{\partial}{\partial \vec{p}} \right\} f_j(\vec{x}, \vec{p}, t) = 0, \quad (24)$$

where the subindex j refers to either the beam or the electrons, and

$$\vec{F}_j = -m_j \gamma_j \omega_{\beta,j}^2 \vec{x}_\perp - e_j \vec{\nabla} \phi + \frac{v_z}{c} \vec{\nabla}_\perp A_z \quad (25)$$

is the force due to external focusing, electric self-fields, and magnetic self-fields. The above Vlasov-Maxwell equations are solved by a perturbative, but fully nonlinear δf formalism, which considers the evolution of a small deviation δf_j from a stationary equilibrium distribution [46,82]:

$$f_j = f_{j,0} + \delta f_j. \quad (26)$$

The numerical solution advances a density weight function together with the particle's phase-space coordinates. The advantage of the δf method is that the noise is reduced by a factor $(\delta f_j / f_{j,0})^2$ compared with a direct nonperturbative solution. The tune spreads induced by nonlinear space charge are automatically included in the Vlasov-Maxwell approach. Numerical solutions are so far restricted to coasting beams, for which a stationary solution is known. Above a threshold, they exhibit unstable dipole modes [82]. They also reveal the existence of a second phase of nonlinear growth which occurs after the initial linear instability for both beam and electrons has saturated, and which strongly increases the beam density perturbation on a long time scale [46,82].

Summarizing the characteristic features of electron-cloud effects for long proton bunches (see also [83]), we note that (1) varied opinions exist concerning the importance and role of the nonlinear space charge, e.g., in [80,82]; (2) the electron oscillation frequency depends on the local beam current and on the local electron density, which strongly increases near the bunch tail—not taken into account in some of the simplified descriptions but probably significant; and (3) a self-consistent treatment of instability and electron generation will likely prove necessary.

As for conventional impedance-driven instabilities, the effect of the electron cloud depends on whether there are less than one or many electron (or resonator) oscillations over the length of the bunch. Following Rumolo [47], we introduce a parameter n denoting the number of vertical oscillations over the full length of the bunch:

$$n = \frac{2\sqrt{\pi} \sigma_z \omega_e}{2\pi c} \approx \left(\frac{2^{1/2} Z N_b \sigma_z r_e}{\pi^{3/2} (\sigma_x + \sigma_y) \sigma_y} \right)^{1/2}. \quad (27)$$

If $n \gg 1$, the bunch can be considered as long, and if $n \ll 1$, as short. Table II illustrates that almost all present or future storage rings operate with “long” bunches, the only possible exception being DAFNE.

Figure 56 illustrates, for a conventional impedance, how the TMCI intensity threshold varies as a function of bunch

TABLE II. Selected storage rings with electron-cloud concerns, the type of stored particles, typical rms bunch length, parameter n defined in the text, and rigidity factor.

Ring	Species	σ_z/c (ns)	n	$Z/(A\gamma)$
DAFNE	Positrons	0.083	0.7	1.88
SPS	Protons	1	1.2	0.036
LHC (inj.)	Protons	0.45	1.6	0.0021
KEKB	Positrons	0.013	1.6	0.27
LHC (top)	Protons	0.25	1.8	0.00013
RHIC	Au ⁷⁹⁺ ions	2.5	3.0	0.0037
PS (store)	Protons	2.5	3.0	0.036
SIS18	U ⁷³⁺ ions	17	7.3	0.25
ISIS	Protons	23	15	0.54
PSR	Protons	54	53	0.54

length. The threshold assumes a minimum close to $n \approx 1/2$ and it increases monotonically for both shorter and longer bunches. Why the bunch length at $n \approx 1/2$ is the most unstable one can be understood from Fig. 57, which shows that the Green-function wakefield changes sign after a distance $\Delta t \approx 1/(2f_r)$; hence for $n \approx 1/2$ the full bunch length matches the first half oscillation of the wake [84]. Figure 58 shows this case in the frequency domain. The modes 0 and -1 are coupled together by the negative resistive impedance and give rise to the TMCI threshold.

Figure 59 illustrates the situation for a long bunch. In this case the two adjacent modes determining the TMCI threshold, m and $m + 1$, are those overlapping the peak of the negative resistive impedance. The corresponding mode number is given by

$$|m| + 1 \approx 8f_r \sigma_z (1 + \omega_{\xi_y} / \omega_r) / c, \quad (28)$$

where

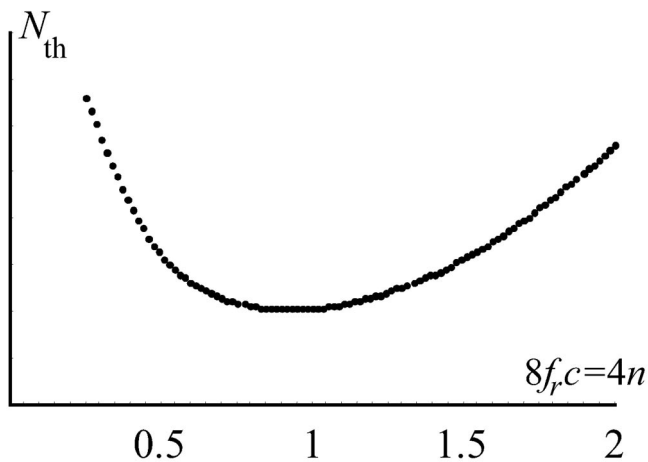


FIG. 56. Intensity threshold for a classical broadband resonator near $n \approx 1/2$ [84,106].

Transverse wake-field

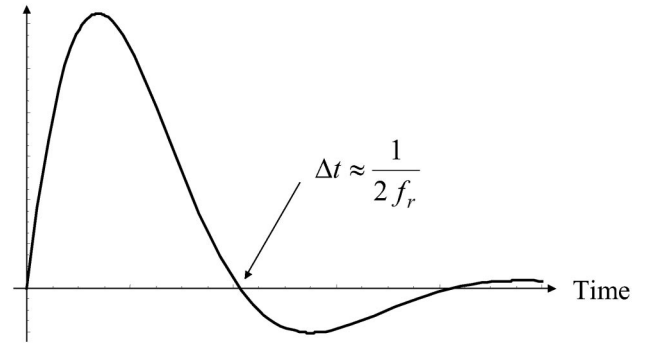


FIG. 57. Transverse Green-function wakefield for a classical broadband resonator as a function of time [84].

$$\omega_{\xi_y} \equiv \left(\frac{\xi_y}{\eta} \right) \omega_\beta \quad (29)$$

denotes the chromatic frequency shift. As a consequence of the change in the relevant mode number with chromaticity, the TMC instability threshold for long bunches increases in proportion to $(1 + \omega_\xi / \omega_r)$. In other words, to achieve a noticeable increase in TMCI threshold the chromatic frequency shift must be comparable to the resonator frequency, which for the electron-cloud case equals the electron oscillation frequency inside the bunch [84]. For short bunches a weaker dependence on chromaticity is expected, since the power spectrum of mode 0 extends well beyond the resonator frequency [84]. We here recall that, when the TMCI theory is applied to the electron-cloud problem, the resonator frequency and the peak impedance depend on the bunch charge (and on the bunch length), so that the threshold expression becomes an implicit equation.

An important difference between the electron-cloud impedance and a conventional impedance is the evolution of the electron-cloud density during the bunch passage (pinch). The pinch arises due to the attracting force of

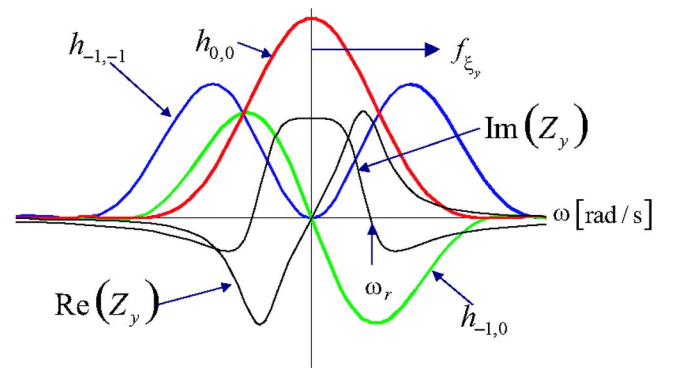


FIG. 58. (Color) Power spectra for the most unstable bunch length with $n \approx 1/2$, as well as the real and imaginary parts of the driving broadband impedance [84].

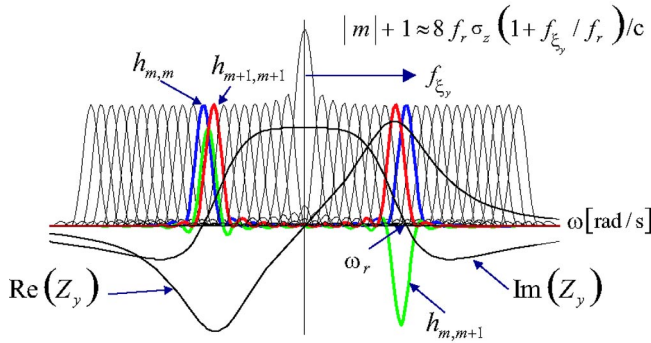


FIG. 59. (Color) Power spectra for a long bunch with $n \gg 1/2$, as well as the real and imaginary parts of the driving broadband impedance [84].

the beam. Electrons in the linear portion of the beam field cross the center of the beam after a quarter oscillation. The nonlinearity at larger amplitudes results in electrons at larger amplitudes “lagging behind.” Typical electron phase-space distributions and their spatial projections are shown in Fig. 60 [85].

In 1999, Furman and Zholents discussed a number of incoherent perturbations resulting from the electron pinch, such as tune spread, beta beating, spurious dispersion, and the excitation of synchrotron resonances [86]. Figures 61 and 62 present some of their classical results for PEP-II. Figure 61 shows the electron transverse density distribution after the bunch passage, and Fig. 62 shows the increase of the density near the beam axis as a function of position along the bunch; in Fig. 62 the electron density is normalized to its initial uniform value.

Figure 63 shows the result of a similar simulation for the LHC at injection energy [87]. In this case, the enhancement of the local density on the beam axis is shown (i.e., without averaging over 1σ). After an initial increase the electron

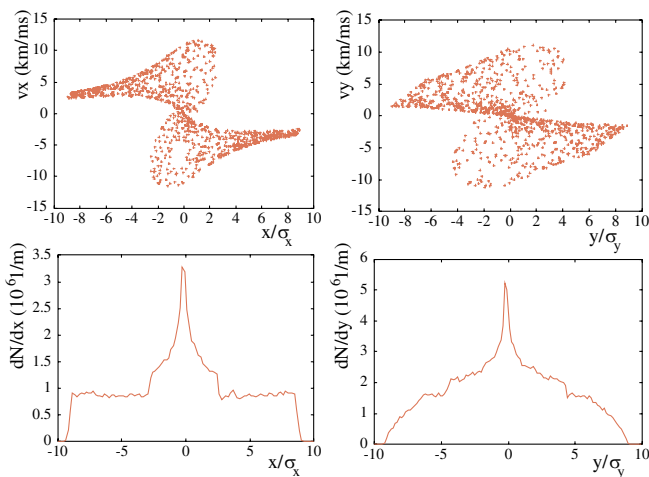


FIG. 60. (Color) Snapshot of horizontal (left) and vertical (right) electron phase space (top) and their projection onto the position axes (bottom) at the end of a bunch passage in the SPS [85].

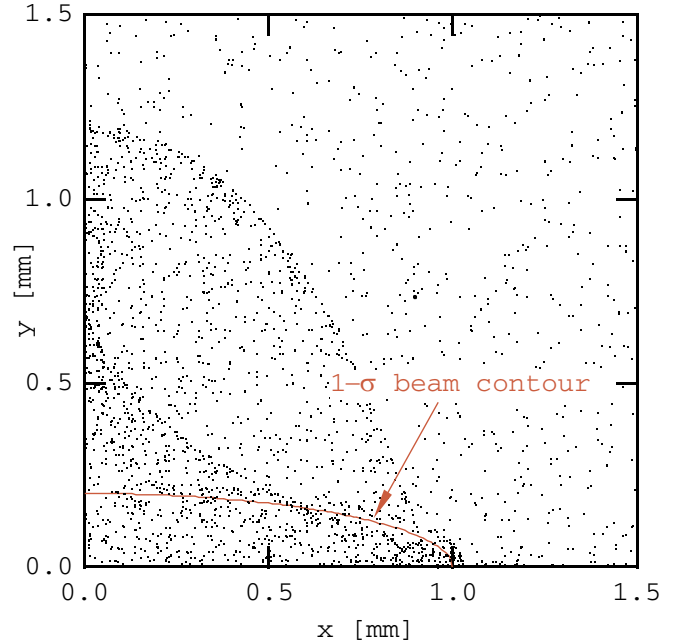


FIG. 61. (Color) Simulated electron distribution for the PEP-II LER pumping straight chamber just after the tail of a bunch has passed [86].

density approximately follows the bunch density profile. Superimposed is a modulation at twice the linear electron oscillation frequency. Without magnetic field, the maximum enhancement for the round LHC beam is about 60.

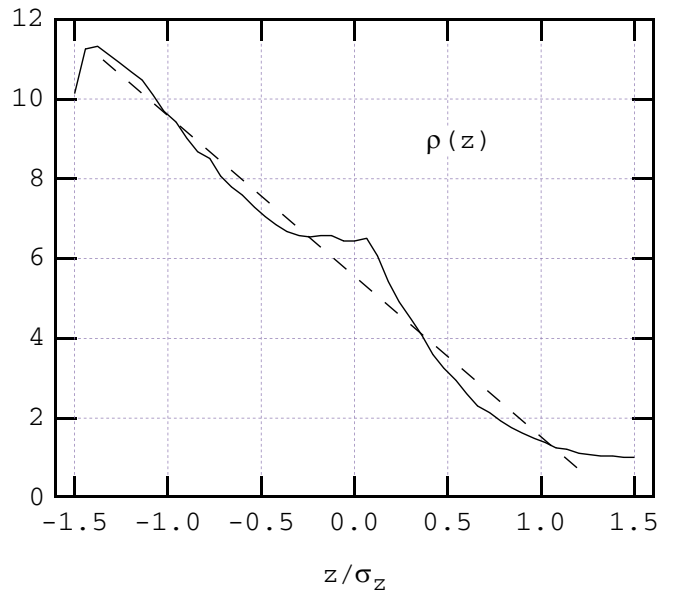


FIG. 62. (Color) Simulated electron density enhancement factor $\rho(z)$ within a 1σ ellipse around the beam axis as a function of the longitudinal position z within the bunch for the PEP-II LER pumping straight chamber; the bunch head is on the right; the straight line is a freehand approximation [86].

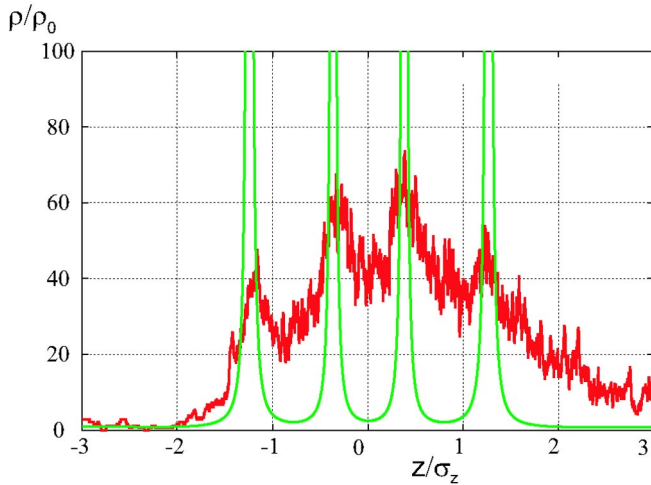


FIG. 63. (Color) Electron-density enhancement (“pinch effect”) at the beam center during the passage of an LHC bunch; the bunch head is on the left; the simulation (red curve) includes the exact nonlinear force; an analytical prediction for a linearized force is superimposed (green line); the intervals between density peaks correspond to half periods of the small-amplitude electron oscillation around the beam center; near the bunch center the density enhancement is about a factor of 50 [87].

The pinched electron distribution should give rise to a large incoherent tune spread, with protons or positron in the center or tail of the bunch and near the beam axis experiencing the largest focusing force from the electrons. Beam particles at the head of the bunch or at large betatron amplitudes are subjected to weaker field and, thus, their tune shift should be smaller. Tune spectra measurements at the KEKB LER, performed with different electron densities, provide strong experimental evidence for the electron-cloud induced vertical tune spread, as is illustrated in Figs. 64 and 65. The electron density was varied by turning on and off the solenoid magnets that cover most of the otherwise field-free regions of the ring.

The electron-induced tune spread was studied in simulations with the HEADTAIL code [88]. For the purpose of extracting accurate tune values for individual beam particles, the pinched electron distribution as a function of longitudinal position along the bunch and the resulting electric fields were computed for a single bunch passage and saved. Then the same fields at a fixed longitudinal location along the bunch were applied on successive turns. This “frozen-field approximation” generates a time-independent Hamiltonian, for which the precise frequency map analysis [89] can be applied [88]. A tune shift of only 0.003 is expected for the unperturbed uniform cloud density, while the pinched cloud at the tail of the bunch induces a tune spread of some 0.05 units, about 20 times larger. The pinched cloud does not only cause a tune spread, but it also excites resonances. Figure 66 reveals beam particles locked to various resonance lines, e.g., to the (0, 3), (1, -4), and tenth order lines. The simulation

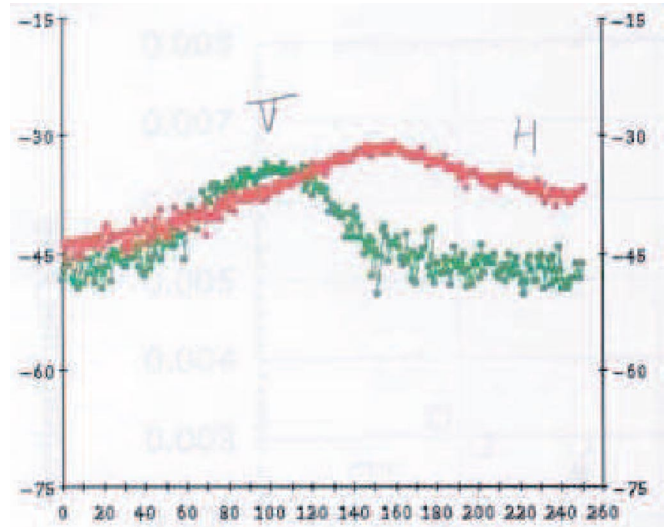


FIG. 64. (Color) Vertical (green) and horizontal (red) tune spectrum detected at the KEKB LER in 2000 or 2001, with solenoids off; the different width of the vertical spectrum as compared with Fig. 65 indicates significant incoherent tune spread [107].

with a frozen potential exhibits much less emittance growth than the simulations for a dynamic two-stream system, which suggests that the incoherent effect of the electron cloud alone is not the dominant source of emittance growth.

An analytical calculation by Perevedentsev of the TMC instability including the incoherent tune shift induced along the bunch due to the electron pinch indicates that the latter has a stabilizing effect and that it can greatly

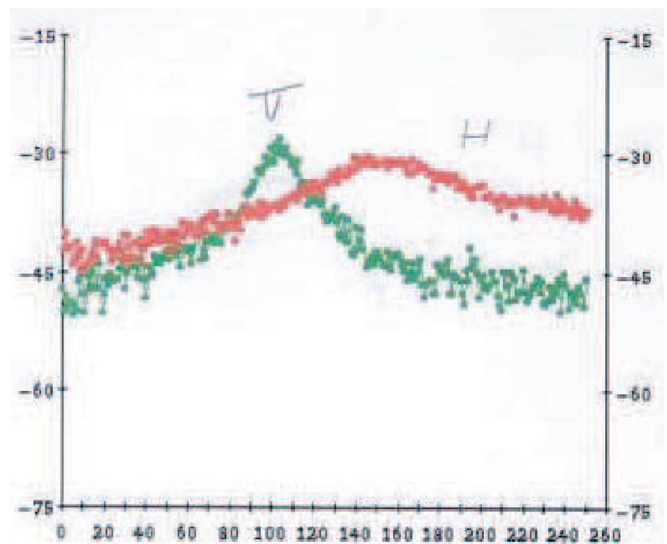


FIG. 65. (Color) Vertical (green) and horizontal (red) tune spectrum detected at the KEKB LER in 2000 or 2001, with solenoids on, reducing electron density near the beam; the vertical tune spread is much narrower than with solenoids off (compare Fig. 64) [107].

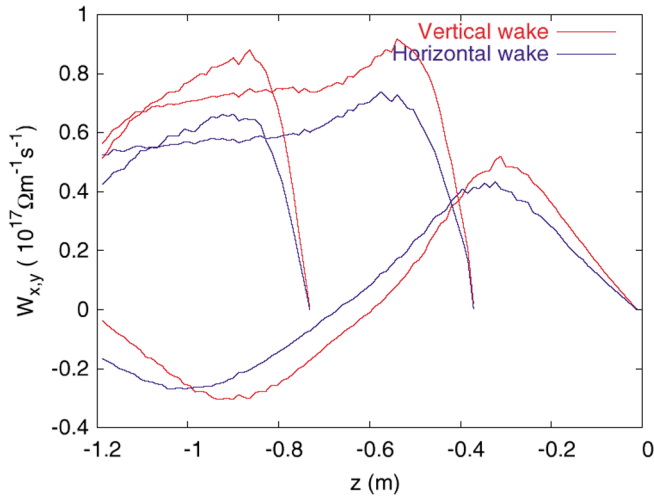


FIG. 70. (Color) Horizontal and vertical dipole wake functions for a uniform SPS bunch obtained by displacing several bunch slices in a field-free region and averaging the resulting forces over the transverse beam size [85].

butions shown in Fig. 72 were generated by Rumolo as initial input densities for single-bunch wakefield calculations. Wakefields corresponding to the different horizontal positions of the two stripes in Fig. 72 are illustrated in Fig. 73. For the same average density of electrons, the amplitude of the vertical wake is greatly reduced as the electron stripes move away from the vicinity of the beam. The horizontal wake is less sensitive to the stripe position; it is also much smaller than the vertical wake in all cases.

Though most of the analytical treatments are based on the notion of a wakefield, it must be noted that the force transmitted by the electron cloud to successive parts of a bunch (or to later bunches) is not a true wakefield in the

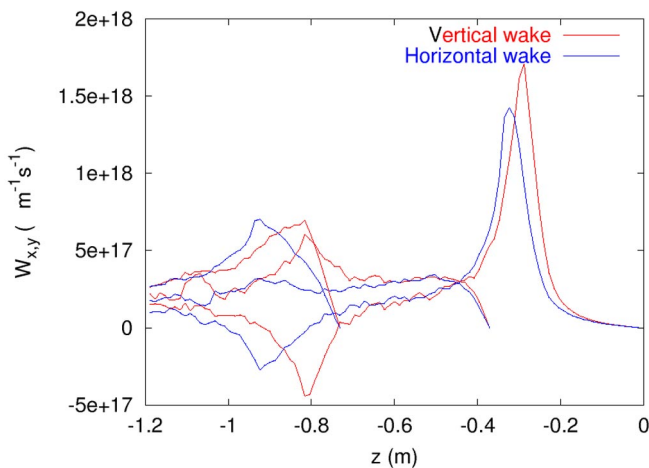


FIG. 71. (Color) Horizontal and vertical dipole wake functions for a uniform SPS bunch obtained by displacing three several bunch slices in a field-free region and computing the resulting force on axis [85].

classical sense. It deviates from the latter in various regards:

- (1) the “electron wake” is not strictly linear in the displacement amplitude (nonlinear force);
- (2) it depends on the intensity, beam size, and bunch length, hence on several beam parameters, while the conventional wakefield for ultrarelativistic beams is independent of beam properties;
- (3) it is not translational invariant, due to the electron pinch during the bunch passage and due to the variation of the electron oscillation frequency with the local beam density;
- (4) the superposition principle does not apply, due to the nonlinear force and due to the memory of previous perturbations stored in the electron motion;
- (5) the wake depends on the transverse position, even if the beam is ultrarelativistic, which is not the case for a classical wake;
- (6) in simulations the effect of the electron wake on the beam emittance varies strongly with the number of “beam-electron interaction points” per turn (see Fig. 49); such dependence is hardly ever observed for a classical impedance (unless a synchrotron resonance is hit).

In view of these significant differences, the conventional formalism should be applied to the electron-cloud instabilities only with great care and it needs to be cross-checked with simulations. So far a few attempts have been made to account for point (3) in the above list: The three- and four-particle models in [53] included a tune shift along the bunch, representing the incoherent tune shift from the electron pinch in a simplified way. Much more groundbreaking is an exact analytical treatment by Perevedentsev, who extended the concept of impedance to cases without translational invariance [72]. The dependence of the “electron wakefield” on the longitudinal location of the driving charge within the bunch can be taken into account by generalizing the notion of the wakefield from one that depends only on the distance between the driving and the test particle, $W_1(z - z')$, to one that independently depends on the positions of these two particles, $W_1(z, z')$. The mathematical framework for this generalization has been worked out in great detail by Perevedentsev [72]. The generalized wake is related to the generalized impedance $\hat{Z}_1(\omega, \omega')$ by a two-dimensional Fourier transform:

$$W_1(z, z') = \iint \frac{d\omega}{2\pi} \frac{d\omega'}{2\pi} \frac{1}{i} \hat{Z}_1(\omega, \omega') e^{i(\omega z - \omega' z')/c}. \quad (30)$$

The wake $W_1(z, z')$ can be obtained from simulations. An example result for the SPS is shown in Fig. 74. The inverse Fourier transform of this two-dimensional wakefield yields the two-dimensional impedance. Two such impedances, for the CERN SPS and the GSI SIS18, are illustrated in Fig. 75. From the generalized impedance, the TMCI threshold can be obtained analytically. The TMCI calcu-

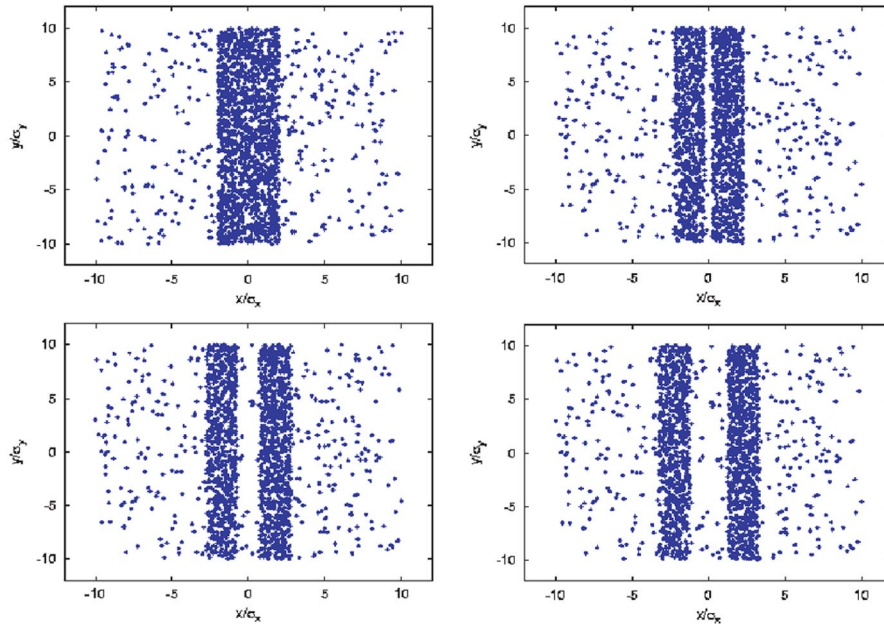


FIG. 72. (Color) Illustration of electron distributions with one or two vertical stripes, representing initial electron densities which may exist in a dipole field; here 10% of the electrons are distributed uniformly, 90% are in the stripes; as shown in Fig. 73, the different stripe distributions yield different wakefields for the same average density [91].

lation proceeds via expansion into a set of orthonormal functions and subsequent solution of a matrix eigenvalue equation [72], just as for the conventional one-dimensional impedance. Only the expression of the matrix elements now involves a double integral over the two-dimensional impedance, rather than a single integral [72].

V. OUTSTANDING QUESTIONS

There are a number intriguing open questions, some of which are possibly crossing the border between accelerator physics and plasma physics. The first question is whether there exist important instability modes that are not of dipolar character. Figure 76 shows evidence for a circular symmetric instability mode found in a two-dimensional plasma simulation modeling the beam-electron interaction

in quasistatic approximation with enforced independence from the transverse azimuth [94]. As illustrated in Fig. 77, strong emittance growth was seen, if the so-called arrival-point, i.e., the point where small-amplitude electrons first cross the beam axis, lies in front of the bunch center. For a Gaussian profile, this condition can also be written as [49]

$$\frac{N_b r_e \sigma_z}{\sigma_r^2} \geq 3.36. \quad (31)$$

As is also shown in Fig. 77, the emittance growth rate was directly proportional to the electron density.

Inspired by the results of [52], the possible existence of monopole-mode instabilities was explored with the HEADTAIL code [88]. Figure 78 presents a typical simulation of emittance growth in the LHC. The three curves refer to three different numbers of equidistant beam-electron

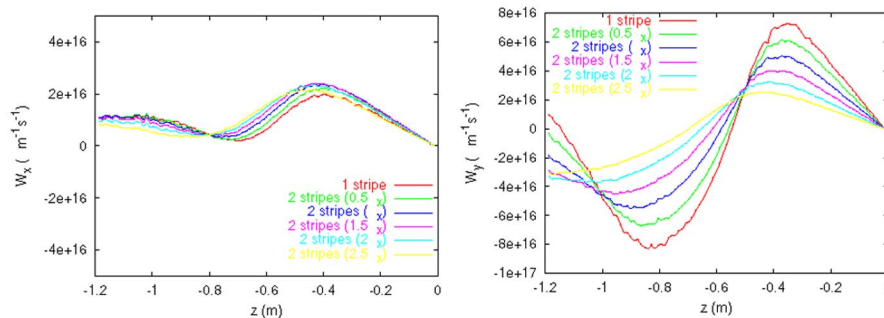


FIG. 73. (Color) Horizontal (left) and vertical (right) averaged dipole wake functions for a Gaussian SPS bunch in a dipole field; the various curves refer to different initial electron distributions (a single $4\sigma_x$ wide vertical stripe, and two $2\sigma_x$ wide stripes located at increasing distances from the center); the different stripe distributions yield different wakefields for the same average density [108].

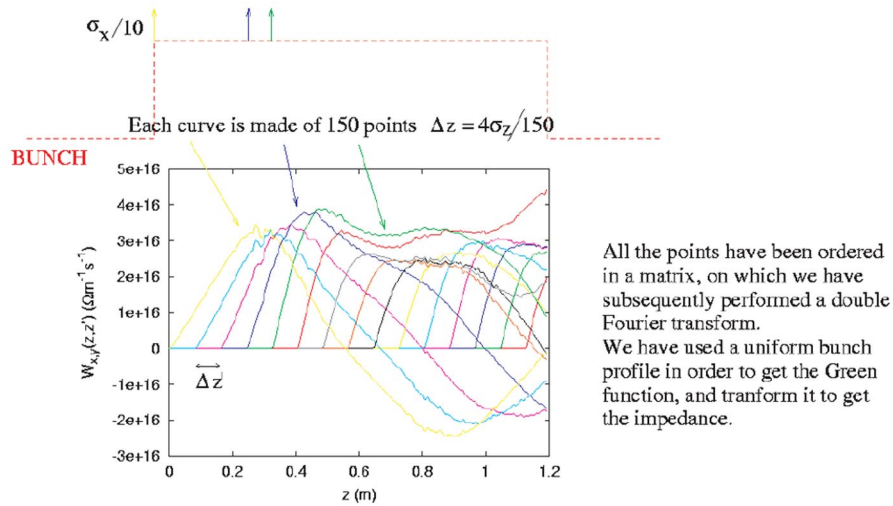


FIG. 74. (Color) Two-dimensional wakefield simulated by Rumolo [91] for a uniform bunch profile in the CERN SPS using the HEADTAIL code; displacing different bunch slices gives rise to nonidentical wakefields that enter into the Fourier transform for the two-dimensional impedance; the bunch head is on the left.

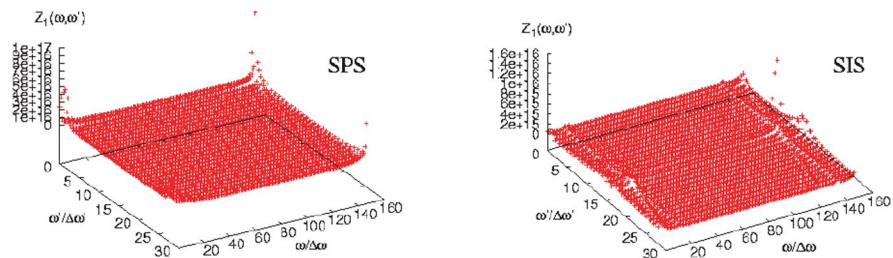


FIG. 75. (Color) Two-dimensional impedance $\hat{Z}_1(\omega, \omega')$ obtained for a uniform bunch profile in the SPS (left) and in the GSI-SIS18 including the effect of a detuned electron cooler (right) [91,109].

interaction points per turn. The emittance growth changes with the number of IPs. The origin of this dependence is not completely understood, but it is most likely related to different resonances being excited.

Figure 79 shows that suppressing the centroid motion of the bunch prior to each IP reduces the emittance growth, if there are several IPs. The reduction is even more pronounced, if not only the bunch-centroid motion is suppressed, but also the centroid motion of each single bunch slice, as is shown in Fig. 80. Finally, the macro-

particle distributions for electrons and beam protons can be perfectly symmetrized, so that for each particle at initial coordinates (x, y) , there are equivalent partners at positions $(-x, y)$, $(x, -y)$, and $(-x, -y)$, which prevents the occur-

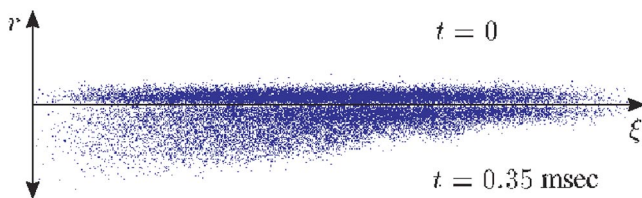


FIG. 76. (Color) Beam distribution in $z - \xi$ plane for $t = 0$ (top) and $t = 0.35$ ms (bottom), without synchrotron motion [52]; $\xi = s - ct$ is the longitudinal distance from the bunch center.

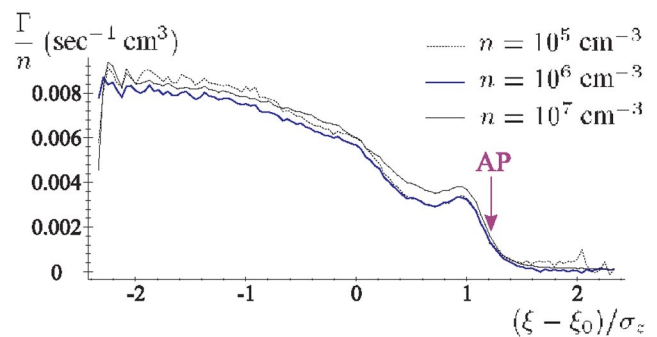


FIG. 77. (Color) Emittance growth rate as a function of longitudinal position within the bunch for three different electron densities, in the absence of synchrotron motion. The beam center corresponds to $\xi = \xi_0$; the arrow shows the “arrival-point location,” which is the point where electrons starting at small amplitudes first and simultaneously cross the beam axis [52].

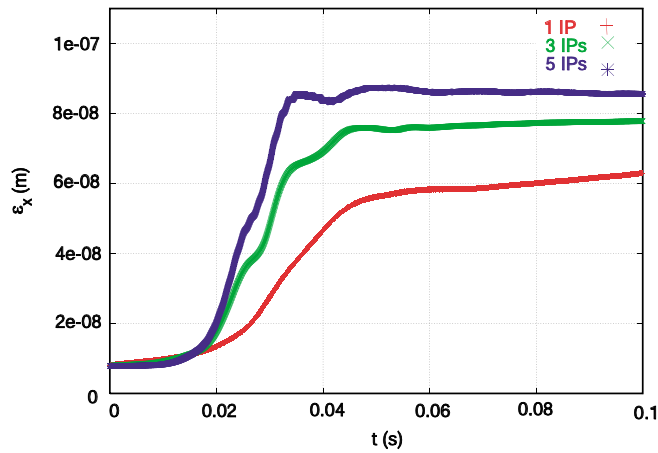


FIG. 78. (Color) Simulated evolution of LHC emittance versus time in seconds for $\rho_e = 6 \times 10^{11} \text{ m}^{-3}$ in a full simulation with fixed phase advances between IPs; the curves correspond to different numbers of electron-beam IPs [88].

rence of any dipolar motion during the collision. With this symmetrization in place, the simulated emittance growth vanishes completely, which is illustrated in Fig. 81. This seems to suggest that, at least in HEADTAIL, there is no noticeable isolated “monopole” or incoherent emittance growth. A small amount of dipolar motion between the beam and the electron cloud appears to be required to cause a measurable emittance blowup [88].

A second open question concerns the possible existence of a second instability regime [29] and, more particularly, the origin of the slow emittance growth, below the TMCI threshold, observed in some simulations [29,40] and possibly at KEKB [95] and PEP-II [40].

A third open question is the effect of a real lattice as compared with a smooth approximation. From space-

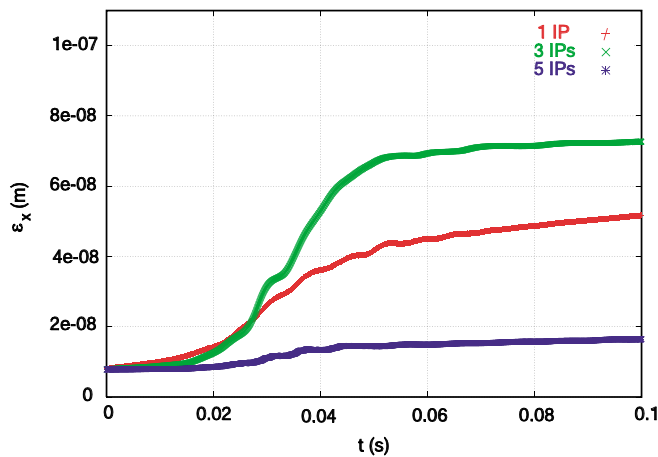


FIG. 79. (Color) Simulated evolution of LHC emittance versus time in seconds for $\rho_e = 6 \times 10^{11} \text{ m}^{-3}$ when the bunch centroid motion is suppressed at each IP; the curves correspond to different numbers of electron-beam IPs [88].

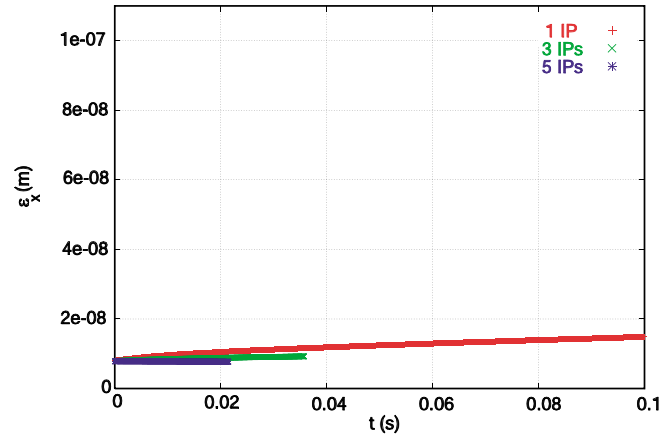


FIG. 80. (Color) Simulated evolution of LHC emittance versus time in seconds for $\rho_e = 6 \times 10^{11} \text{ m}^{-3}$ when the bunch-slice centroid motion is suppressed at each IP; the curves correspond to different numbers of electron-beam IPs [88].

charge simulations it is known that the emittance growth for a real lattice can be much larger than that for a smooth optics [96]. Whether a similar statement holds for the electron cloud remains to be investigated.

Also, more realistic electron distributions could alter the simulation result. This point does not only refer to the transverse stripes mentioned above, but also to longitudinal discontinuities, e.g., the existence of an electron cloud inside a certain type of magnet and a smaller cloud or no cloud at all in adjacent beam-pipe regions.

A fifth question is whether we should look out for approaches that are superior to PIC calculations [97]. Specifically, this might be necessary if the slow emittance growth should turn out to be a numerical artifact. One possible path to reduce artificial emittance growth from simulation noise could be to apply the δf technique which

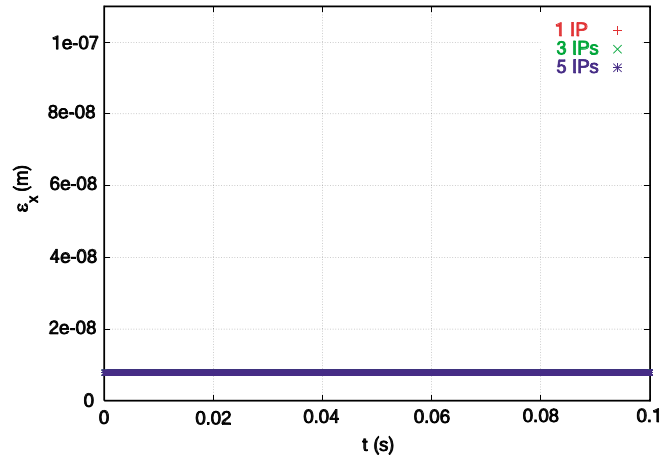


FIG. 81. (Color) Simulated evolution of LHC emittance versus time in seconds for $\rho_e = 6 \times 10^{11} \text{ m}^{-3}$ when the beam and electron macroparticles are perfectly symmetrized; the curves correspond to different numbers of electron-beam IPs [88].

is used in the BEST code or a variant thereof. This, however, may require an *a priori* knowledge of a stationary distribution.

Finally, the sixth and last question addresses the possible existence and importance of longitudinal plasma waves. In [98], Parkhomchuk and co-workers attempt to explain the lifetime reduction experienced by proton bunches interacting on successive turns with a magnetized electron beam (namely the Tevatron Electron Lens, or short, TEL) in the Fermilab Tevatron by either of two mechanisms: scattering off plasma fluctuations excited by individual protons or longitudinal wakefields excited in the electron-beam plasma. Figure 82 displays longitudinal plasma waves excited by a passing proton bunch in the electron beam detected by a beam-position pickup. The first small “wobble” corresponds to the polarization field traveling with the proton beam, the second and third, larger peaks are the so-called fast and slow waves. These waves are excited as the bunch enters and leaves the electron beam. This observation may suggest that longitudinal discontinuities in the electron cloud, which are certainly abundant in a storage ring, could lead to much larger longitudinal wakefields than those expected for a longitudinally uniform electron cloud. Figure 83 illustrates the longitudinal wake predicted by an analytical model. The electron-density variation also obtained from this model looks quite similar to the measurement in Fig. 82 [98].

On March 1, 2004, another experiment with the TEL was performed [99]. Here the electron beam was moved transversely across the positions of the proton and antiproton beams, respectively. The scanned positions are illustrated in Fig. 84. Figure 85 shows a contour plot of the

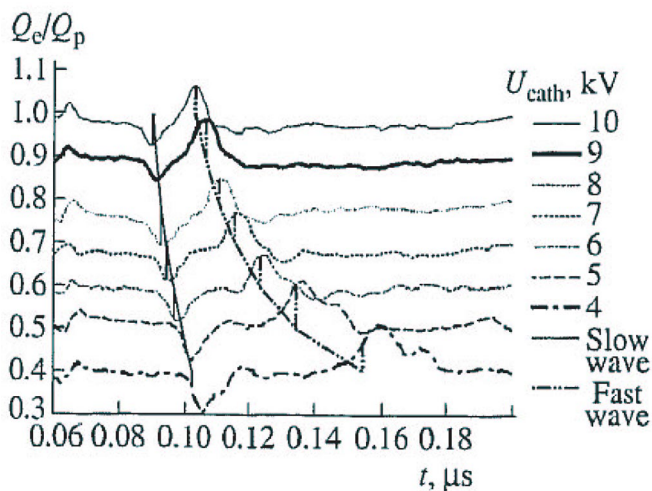


FIG. 82. (Color) Charge disturbance in the TEL electron beam detected by a pickup, as a function of time over the first 200 ns after a proton-bunch transit; the different curves refer to various TEL electron-beam energies (cathode voltages); they are separated by 0.1 units in the vertical direction [98]; a fast wave and a slow wave are evident.

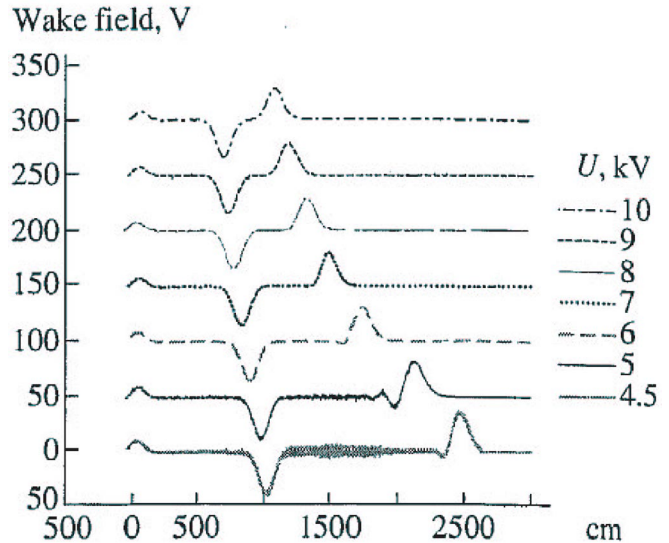


FIG. 83. (Color) Potential of the longitudinal waves in the TEL electron beam after the passage of the proton bunch computed by a flat-disk model; three characteristic features are noticeable: a near zone around 0 cm, caused by polarization and local plasma oscillation, a fast wave (excited when the proton bunch enters into the electron beam), and a slow wave (excited where the proton bunch leaves the electron beam) [98].

proton loss rate as a function of the two-dimensional transverse position of the electron beam. The position with maximum loss rate corresponds to the location of the proton beam. Similar plots were obtained for the antiprotons. Figure 86 shows that the antiproton loss rate decreases with the third inverse power of the distance between electron and antiproton beams. Figure 87 illustrates that for the proton beam, whose intensity was about 10 times higher and which showed greater losses than the

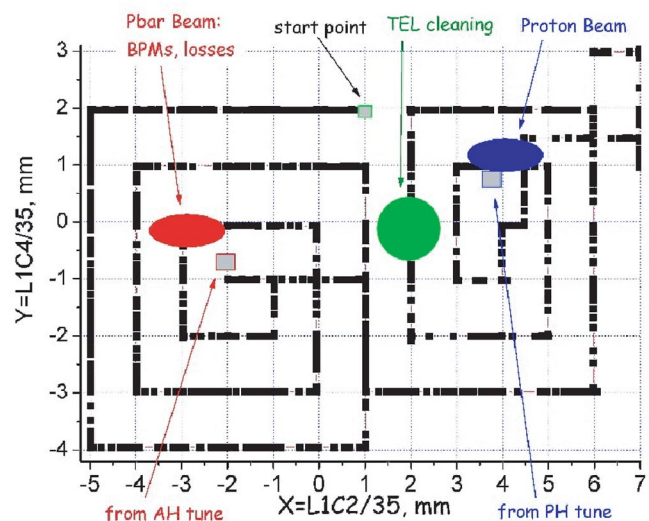


FIG. 84. (Color) Summary of TEL position scan; beam sizes are approximately to scale (Shiltsev) [99].

Proton losses vs e-beam position

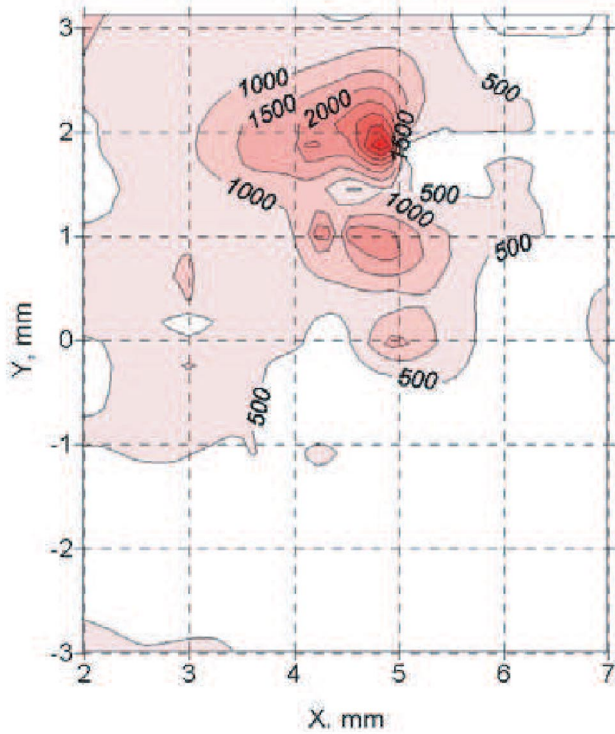


FIG. 85. (Color) Proton losses versus TEL position (Shiltsev) [99].

antiprotons, the losses occurred mainly longitudinally, which might be consistent with the effect of longitudinal plasma wakefields as suggested by Parkhomchuk.

To estimate the expected field amplitude of possibly excited plasma waves, we note that, for a typical electron density of 10^{12} m^{-3} , the plasma frequency

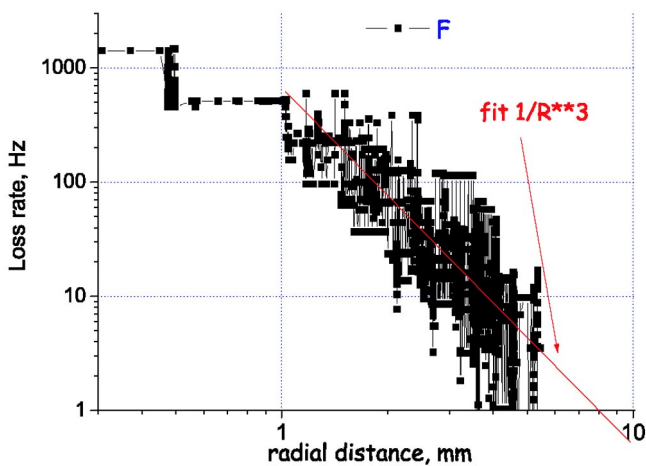


FIG. 86. (Color) Antiproton loss rate as a function of TEL distance, exhibiting an inverse cubic dependence (Shiltsev) [99].

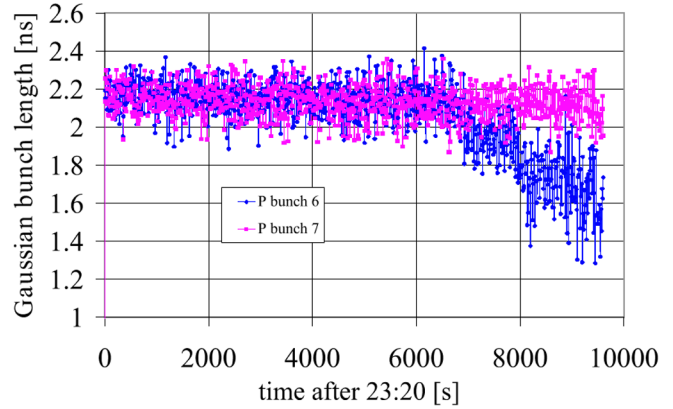


FIG. 87. (Color) Bunch length from a Gaussian fit to wall-current monitor signal as a function of time for proton bunches P6 and P7; bunch P6, which interacts with the TEL, is shaved longitudinally [99].

$$\omega_p = \sqrt{4\pi r_e c^2 \rho_e} \quad (32)$$

is of the order $6 \times 10^7 \text{ s}^{-1}$. For cold relativistic oscillations the electric field at the wave breaking limit can be approximated by [100,101]

$$E_{\text{max}} \approx \frac{\sqrt{2\gamma} m_e \omega_p c}{e}. \quad (33)$$

For example, for phase velocities equal to the beam velocity, and $\gamma \approx 5000$, the cold wave breaking limit is 10 MV/m, while the nonrelativistic limit [100,102] is about 100 kV/m.

ACKNOWLEDGMENTS

I would like to thank R. Macek and M. Furman for inviting this review talk on single-bunch instabilities at the ELOUD'04 workshop. Warm thanks also go to G. Arduini, V. Baglin, G. Bellodi, E. Benedetto, M. Blaskiewicz, K. Cornelis, V. Danilov, V. Dudnikov, H. Fukuma, Y. Funakoshi, M. Furman, A. Ghalam, Z. Y. Guo, S. Heifets, T. Ieiri, M. Jiménez, D. Kaltchev, T. Katsouleas, R. Macek, E. Métral, K. Ohmi, K. Oide, E. Perevedentsev, M. Pivi, T. Raubenheimer, B. Richter, A. Rossi, F. Ruggiero, G. Rumolo, D. Schulte, V. Shiltsev, C. Vaccarezza, J. Wang, R. Wanzenberg, A. Wolski, X.-L. Zhang, M. Zobov, and many other colleagues who shared their insights with me in numerous discussions, providing invaluable information and much of the material presented in this paper. I am grateful to M. Furman for a careful reading of the manuscript and many helpful comments.

[1] K. Ohmi, in *Proceedings of ELOUD'04, Napa, CA* (CERN, to be published), http://mafurman.lbl.gov/ELOUD04_proceedings/.

- [2] M. Izawa, Y. Sato, and T. Toyomasu, *Phys. Rev. Lett.* **74**, 5044 (1995).
- [3] Z. Y. Guo, H. Huang, S. P. Li, D. K. Liu, Y. Luo, L. Ma, Q. Qin, L. F. Wang, J. Q. Wang, S. H. Wang, J. W. Xu, K. R. Ye, C. Zhang, F. Zhou, Y. H. Chin, H. Fukuma, S. Hiramatsu, M. Izawa, T. Kasuga, E. Kikutani, Y. Kobayashi, S. Kurokawa, K. Ohmi, Y. Sato, Y. Suetsugu, M. Tobiyama, K. Tsukamoto, and K. Yokoya, in *Proceedings of the Particle Accelerator Conference, New York, 1999* (IEEE, Piscataway, NJ, 1999).
- [4] S. S. Win, H. Fukuma, E. Kikutani, and M. Tobiyama, in *Proceedings of the Asian Particle Accelerator Conference, Beijing, 2001* (Institute of High Energy, Physics, Beijing, 2001).
- [5] G. Arduini, in *Proceedings of Chamonix XI, 2001* (Report No. CERN-SL-2001-003 DI, 2001).
- [6] K. Cornelis, in *Proceedings of ELOUD'02, Geneva* (Report No. CERN-2002-001, 2002).
- [7] K. Ohmi, *Phys. Rev. Lett.* **75**, 1526 (1995).
- [8] M. A. Furman and G. R. Lambertson, in *Proceedings of the International Workshop on Multibunch Instabilities in Future Electron and Positron Accelerators (MBI'97), Tsukuba*, edited by Y. H. Chin, KEK Proceedings Vol. 97-17 (KEK, Tsukuba, 1997).
- [9] K. Ohmi, in *Proceedings of the International Workshop on Multibunch Instabilities in Future Electron and Positron Accelerators (MBI'97), Tsukuba* (Ref. [8]).
- [10] S. S. Win, H. Fukuma, K. Ohmi, and S.-I. Kurokawa, in *Proceedings of ELOUD'02, Geneva* (Ref. [6]).
- [11] D. Schulte, in *Proceedings of ELOUD'04, Napa, CA* (Ref. [1]).
- [12] G. Budker, G. Dimov, and V. Dudnikov, in *Proceedings of the International Symposium on Electron and Positron Storage Rings, Saclay, France, 1966* (Saclay, Paris, 1966), Article No. VIII-6-1.
- [13] G. Budker, G. Dimov, and V. Dudnikov, *Sov. At. Energy* **22**, 384 (1967).
- [14] V. Dudnikov, in *Proceedings of the Particle Accelerator Conference, Chicago, 2001* (IEEE, Piscataway, NJ, 2001).
- [15] G. Budker, G. Dimov, V. Dudnikov, and V. Shamovsky, in *Proceedings of the International Conference on High Energy Accelerators, Cambridge, MA, 1967* (CEA, Cambridge, MA, 1967).
- [16] Yu. I. Belchenko, G. Budker, G. E. Derevyankin, G. Dimov, V. Dudnikov, G. V. Roslyakov, V. E. Chupriyanov, and V. G. Shamovsky, in *Proceedings of the Xth International Conference on Particle Accelerators, Protvino, 1977* (Protvino Institute of High Energy Physics, Serpukhov, 1977), Vol. 2, p. 287.
- [17] B. V. Chirikov, *Sov. At. Energy* **19**, 1149 (1965).
- [18] J. H. Martin, R. A. Winje, R. H. Hilden, and F. E. Mills, in *Proceedings of the 5th International Conference on High Energy Accelerators, Frascati, 1965* (CNEN, Rome, 1966), p. 347.
- [19] J. H. Martin, R. A. Winje, and R. C. Trendler, in *Proceedings of the International Conference on High Energy Accelerators, Cambridge, MA, 1967* (Ref. [15]), p. 356.
- [20] E. C. Raka, in *Proceedings of the International Conference on High Energy Accelerators, Cambridge, MA, 1967* (Ref. [15]), p. 428.
- [21] H. A. Grunder and G. R. Lambertson, in *Proceedings of the 8th International Conference on High Energy Accelerators, Geneva, 1971* (CERN, Geneva, 1971).
- [22] R. Calder, E. Fischer, O. Gröbner, and E. Jones, in *Proceedings of the 9th International Conference on High Energy Accelerators, Stanford, 1974* (A.E.C., Washington, DC, 1975), pp. 70-74.
- [23] D. Neuffer, E. Colton, D. Fitzgerald, T. Hardek, R. Hutson, R. Macek, M. Plum, H. A. Thiessen, and T. S. Wang, *Nucl. Instrum. Methods Phys. Res., Sect. A* **321**, 1 (1992).
- [24] R. L. Macek, A. Browman, D. Fitzgerald, R. McCrady, F. Merrill, M. Plum, T. Spickermann, T. S. Wang, J. Griffin, K. Y. Ng, D. Wildman, K. Harkay, R. Kustom, and R. Rosenberg, in *Proceedings of the Particle Accelerator Conference, Chicago, 2001* (Ref. [14]), p. 688.
- [25] M. Blaskiewicz, in *Workshop on Instabilities of High Intensity Hadron Beams in Rings*, edited by T. Roser and S. Y. Zhang, AIP Conf. Proc. No. 496 (AIP, New York, 1999).
- [26] K. Akai, N. Akasaka, K. Bane, A. Enomoto, J. Flanagan, H. Fukuma, Y. Funakoshi, K. Furukawa, J. Haba, S. Hiramatsu, K. Hoyosama, N. Huang, T. Ieiri, N. Iida, T. Kamitani, S. Kato, M. Kikuchi, E. Kikutani, H. Koiso, M. Masuzawa, T. Matsumoto, S. Michizono, T. Mimashi, T. Nakamura, Y. Ogawa, K. Ohmi, Y. Ohnishi, S. Ohsawa, N. Ohuchi, K. Oide, D. Pestrikov, K. Satoh, M. Suetake, Y. Suetsugu, T. Suwada, M. Tawada, M. Tejima, M. Tobiyama, S. Uno, N. Yamamoto, M. Yoshida, S. Yoshimoto, and F. Zimmermann, in *Proceedings of the International Workshop on e^+e^- Factories ("Factories99"), Tsukuba*, KEK Proceedings Vol. 99-24 (KEK, Tsukuba, 2000).
- [27] F. Zimmermann, Report No. CERN SL-Note-2000-004 AP, 2000.
- [28] K. Ohmi and F. Zimmermann, *Phys. Rev. Lett.* **85**, 3821 (2000).
- [29] E. Benedetto, D. Schulte, F. Zimmermann, and G. Rumolo, in *Proceedings of ELOUD'04, Napa, CA* (Ref. [1]).
- [30] H. Fukuma, in *Proceedings of ELOUD'02, Geneva* (Ref. [6]).
- [31] H. Fukuma, in *Proceedings of the ICFA Workshop on e^+e^- Factories, 2003 ("Factories03"), Stanford, CA*, <http://wwwconf.slac.stanford.edu/icfa03/>.
- [32] W. Kozanecki, in *Proceedings of the ICFA Workshop on e^+e^- Factories, 2003 ("Factories03"), Stanford, CA* (Ref. [31]).
- [33] J. Fox, in *Proceedings of the ICFA Workshop on e^+e^- Factories, 2003 ("Factories03"), Stanford, CA* (Ref. [31]).
- [34] E. Métral, in *Proceedings of ELOUD'02, Geneva* (Ref. [6]).
- [35] G. Arduini, in *Proceedings of the Particle Accelerator Conference, Portland OR, 2003* (IEEE, Piscataway, NJ, 2003).
- [36] R. Cappi, M. Giovannozzi, E. Métral, G. Métral, G. Rumolo, and F. Zimmermann, *Phys. Rev. ST Accel. Beams* **5**, 094401 (2002).

- [37] M. Giovannozzi, E. Métral, G. Métral, G. Rumolo, and F. Zimmermann, *Phys. Rev. ST Accel. Beams* **5**, 094401 (2002).
- [38] Z.Y. Guo, Y.D. Liu, Q. Qin, and J.Q. Wang, in *Proceedings of the Asian Particle Accelerator Conference (APAC 2004), Gyeongju, Korea, 2004*, <http://apac04.postech.ac.kr/index.htm>.
- [39] M. Zobov and C. Vaccarezza (private communication); see also C. Vaccarezza, in *Proceedings of ELOUD'04, Napa, CA* (Ref. [1]).
- [40] Y. Cai, in *Proceedings of ELOUD'02, Geneva* (Ref. [6]).
- [41] G. Rumolo and F. Zimmermann, in *Proceedings of the Particle Accelerator Conference, Chicago, 2001* (Ref. [14]), p. 1886.
- [42] K. Ohmi, in *Proceedings of the Particle Accelerator Conference, Chicago, 2001* (Ref. [14]), p. 1895.
- [43] G. Rumolo and F. Zimmermann, Report No. CERN-SL-Note-2002-036 AP, 2002.
- [44] G. Rumolo, A.Z. Ghalam, T. Katsouleas, C.K. Huang, V.K. Decyk, C. Ren, W.B. Mori, F. Zimmermann, and F. Ruggiero, *Phys. Rev. ST Accel. Beams* **6**, 081002 (2003).
- [45] T.-S.F. Wang, in *Proceedings of the Particle Accelerator Conference, Dallas, TX, 1995* (IEEE, Piscataway, NJ, 1995).
- [46] H. Qin, E. A. Startsev, and R. C. Davidson, *Phys. Rev. ST Accel. Beams* **6**, 014401 (2003).
- [47] G. Rumolo, E. Benedetto, U. Iriso, and F. Zimmermann, *ICFA Beam Dynamics Newsletter* **33**, 29 (2004).
- [48] M. Bassetti and G. A. Erskine, Report No. CERN-ISR-TH/80-06, 1980.
- [49] C. K. Huang, V. Decyk, S. Wang, E. S. Dodd, C. Ren, W. B. Mori, T. Katsouleas, and T. Antonsen Jr., in *Proceedings of the Particle Accelerator Conference, Chicago, 2001* (Ref. [14]).
- [50] P. Mugli, M. J. Hogan, B. E. Blue, C. E. Connell, R. H. Siemann, D. Walz, R. A. Assmann, C. E. Clayton, F.-J. Decker, E. S. Dodd, R. H. Iverson, C. Joshi, T. C. Katsouleas, S. Lee, K. A. Marsh, W. B. Mori, P. Raimondi, and S. Wang, in *Proceedings of the Particle Accelerator Conference, Chicago, 2001* (Ref. [14]).
- [51] D. H. Whittum, W. M. Sharp, S. S. Yu, M. Lampe, and G. Joyce, *Phys. Rev. Lett.* **67**, 991 (1991).
- [52] K. V. Lotov and G. Stupakov, in *Proceedings of the European Particle Accelerator Conference, Paris, 2002* (EPS, Geneva, 2002).
- [53] G. Rumolo and F. Zimmermann, in *Proceedings of the Two-Stream Instabilities Workshop, Tsukuba, 2001* [Report No. CERN-SL-2001-067 (AP), 2001].
- [54] K. Ohmi, S. Heifets, and F. Zimmermann, in *Proceedings of the Asian Particle Accelerator Conference, Beijing, 2001* (Ref. [4]).
- [55] D. Chen, A. Chang, M. Pivi, and T. Raubenheimer, Report No. LCC-0126, SLAC-TN-05-051, 2003.
- [56] D. Bates (unpublished).
- [57] G. Arduini, *Proceedings of ELOUD'04, Napa, CA* (Ref. [1]).
- [58] F. Zimmermann, LHC Project Report No. 95, 1997.
- [59] S. Heifets, in *Proceedings of ELOUD'02, Geneva* (Ref. [6]).
- [60] F. Zimmermann, G. Rumolo, and K. Ohmi, *ICFA Beam Dynamics Newsletter* **33**, 14 (2004).
- [61] F. Zimmermann and G. Rumolo, in *Proceedings of the Asian Particle Accelerator Conference, Beijing, 2001* (Ref. [4]).
- [62] F. Zimmermann, Report No. CERN-SL-Note-2000-004 AP, 2000.
- [63] T. O. Raubenheimer and F. Zimmermann, *Phys. Rev. E* **52**, 5487 (1995).
- [64] K. Ohmi, F. Zimmermann, and E. Perevedentsev, *Phys. Rev. E* **65**, 016502 (2002).
- [65] F. Zimmermann, in *Proceedings of the Particle Accelerator Conference, Chicago, 2001* (Ref. [14]).
- [66] B. Zotter, Report No. CERN/ISR-TH/82-10, 1982.
- [67] G. Rumolo, F. Zimmermann, H. Fukuma, K. Ohmi, in *Proceedings of the Particle Accelerator Conference, Chicago, 2001* (Ref. [14]).
- [68] R. D. Ruth and J. M. Wang, in *Proceedings of the 1981 Particle Accelerator Conference, Washington, DC* (IEEE, Piscataway, NJ, 1981).
- [69] D. Pestrikov, in *Proceedings of the ICFA Beam Dynamics Workshop on Collective Effects in Short Bunches, Tsukuba, 1991* (Report No. KEK-90-021, 1991).
- [70] P. Kernel, R. Nagaoka, J. L. Revol, and G. Besnier, in *Proceedings of the European Particle Accelerator Conference, Vienna, 2000* (EPS, Geneva, 2000).
- [71] K. Ohmi, T. Toyama, and C. Ohmori, in *Proceedings of ELOUD'02, Geneva* (Ref. [6]).
- [72] E. Perevedentsev, in *Proceedings of ELOUD'02, Geneva* (Ref. [6]).
- [73] A. W. Chao, *Physics of Collective Beam Instabilities in High Energy Accelerators* (Wiley, New York, 1993).
- [74] G. Rumolo and F. Zimmermann, in *Proceedings of the Two-Stream Instabilities Workshop, Tsukuba, 2001* (Ref. [53]).
- [75] See footnote 31 on p. 198 of Ref. [73].
- [76] K. Ohmi and A. W. Chao, in *Proceedings of ELOUD'02, Geneva* (Ref. [6]).
- [77] T.-S. Wang, P. Channell, R. J. Macek, and R. C. Davidson, *Phys. Rev. ST Accel. Beams* **6**, 014204 (2003).
- [78] P. Channell, *Phys. Rev. ST Accel. Beams* **5**, 114401 (2002).
- [79] S. Heifets, Report No. SLAC-PUB-6959; *Proceedings of CEIBA95, Tsukuba, 1995*, KEK Proceedings Vol. 96-6 (KEK, Tsukuba, 1995).
- [80] M. Blaskiewicz, M. A. Furman, M. Pivi, and R. J. Macek, *Phys. Rev. ST Accel. Beams* **6**, 014203 (2003).
- [81] M. Blaskiewicz, *Phys. Rev. ST Accel. Beams* **4**, 044202 (2001).
- [82] H. Qin, in *Proceedings of the Two-Stream Instabilities Workshop, Tsukuba, 2001* (Ref. [53]).
- [83] M. Blaskiewicz, *ICFA Beam Dynamics Newsletter* **33**, 77 (2004).
- [84] E. Métral, in *Proceedings of ELOUD'02, Geneva* (Ref. [6]).
- [85] G. Rumolo and F. Zimmermann, *Phys. Rev. ST Accel. Beams* **5**, 121002 (2002).
- [86] M. A. Furman and A. A. Zholents, in *Proceedings of the Particle Accelerator Conference, New York, 1999* (Ref. [3]), p. 1794.

- [87] E. Benedetto, in *Proceedings of ELOUD'04, Napa, CA* (Ref. [1]).
- [88] E. Benedetto, D. Schulte, F. Zimmermann, K. Ohmi, Y. Papaphilippou, and G. Rumolo, in *Proceedings of the Particle Accelerator Conference, Portland OR, 2003* (Ref. [35]).
- [89] J. Laskar, *Astron. Astrophys.* **198**, 341 (1988).
- [90] V. Danilov, *Phys. Rev. ST Accel. Beams* **1**, 041301 (1998).
- [91] G. Rumolo, in *Mini-workshop on SPS Scrubbing Results and Implications for the LHC, 2002* (CERN, Geneva, 2002).
- [92] F. Zimmermann, in *Proceedings of Chamonix XII* (Report No. CERN-AB-2003-008 ADM, 2003).
- [93] J.M. Jiménez, G. Arduini, P. Collier, G. Ferioli, B. Henrist, N. Hilleret, L. Jensen, K. Weiss, and F. Zimmermann, LHC-Project-Report-632, 2003.
- [94] During the ELOUD'04 workshop G. Stupakov mentioned that this simulation contained an error.
- [95] H. Fukuma, K. Akai, N. Akasaka, A. Enomoto, J.W. Flanagan, Y. Funakoshi, K. Furukawa, S. Hiramatsu, K. Hoyosama, T. Ieiri, N. Iida, T. Kamitani, S. Kato, M. Kikuchi, E. Kikutani, H. Koiso, T. Kubo, S. Kurokawa, T. Mitsuhashi, M. Masuzawa, T. Matsumoto, T. Mimashi, T. Nakamura, Y. Ogawa, K. Ohmi, Y. Ohnishi, S. Ohsawa, N. Ohuchi, K. Oide, K. Satoh, M. Suetake, Y. Suetsugu, T. Suwada, M. Tawada, M. Tejima, M. Tobiyama, S. Uno, N. Yamamoto, M. Yoshida, M. Yoshioka, S. Yoshimoto, E. Perevedentsev, and F. Zimmermann, in *Proceedings of HEACC 2001, Tsukuba*, <http://conference.kek.jp/heacc2001/>.
- [96] K. Ohmi (private communication).
- [97] In a recent FNAL seminar on “string calculations for space-charge,” R. Talman advocated alternative computing approaches.
- [98] V.V. Parkhomchuk, V.B. Reva, and V.D. Shiltsev, *Tech. Phys.* **48**, 1042 (2003).
- [99] P. Lebrun, T. Sen, V. Shiltsev, X.L. Zhang, and F. Zimmermann, Report No. CERN-AB-Note-2004-041, 2004.
- [100] T. Katsouleas and W. Mori, *Phys. Rev. Lett.* **61**, 1 (1988).
- [101] A.I. Akhiezer and R.V. Polovin, *Zh. Eksp. Teor. Fiz.* **30**, 915 (1956) [*Sov. Phys. JETP* **3**, 696 (1956)].
- [102] J.M. Dawson, *Phys. Rev.* **113**, 383 (1959).
- [103] J. Flanagan, H. Fukuma, S. Hiramatsu, H. Ikeda, and T. Mitsuhashi (private communication).
- [104] F.-J. Decker, in *Proceedings of ELOUD'02, Geneva* (Ref. [6]).
- [105] G. Rumolo and F. Zimmermann, in *Proceedings of Chamonix XI, 2001* (Ref. [5]).
- [106] E. Métral, Report No. CERN/PS 2001-035 (AE), 2001.
- [107] T. Ieiri and H. Fukuma (private communication).
- [108] G. Rumolo and F. Zimmermann, in *Proceedings of the European Particle Accelerator Conference, Paris, 2002* (Ref. [52]).
- [109] G. Rumolo, F. Zimmermann, O. Boine-Frankenheim, and I. Hofmann, in *Proceedings of ELOUD'02, Geneva* (Ref. [6]).